

# Nucleon Resonance Electroexcitation Amplitudes and Emergent Hadron Mass

Daniel S. Carman <sup>1,†</sup>, Ralf W. Gothe <sup>2,†</sup>, Victor I. Mokeev <sup>1,†</sup>, and Craig D. Roberts <sup>3,4,†</sup>\*

<sup>1</sup> Jefferson Laboratory, 12000 Jefferson Ave., Newport News, VA 23606, USA

<sup>2</sup> University of South Carolina, Department of Physics and Astronomy, 712 Main St., Columbia, SC 29208, USA

<sup>3</sup> School of Physics, Nanjing University, Nanjing, Jiangsu 210093, China

<sup>4</sup> Institute for Nonperturbative Physics, Nanjing University, Nanjing, Jiangsu 210093, China

\* Correspondence – all authors:

carman@jlab.org (D. S. Carman); gothe@sc.edu (R. W. Gothe); mokeev@jlab.org (V. I. Mokeev);

cdroberts@nju.edu.cn (C. D. Roberts)

† These authors contributed equally to this work.

**Abstract:** Understanding the strong interaction dynamics that govern the emergence of hadron mass (EHM) represents a challenging open problem in the Standard Model. In this paper we describe new opportunities for gaining insight into EHM from results on nucleon resonance ( $N^*$ ) electroexcitation amplitudes (*i.e.*  $\gamma_v p N^*$  electrocouplings) in the mass range up to 1.8 GeV for virtual photon four-momentum squared (*i.e.* photon virtualities  $Q^2$ ) up to 7.5 GeV<sup>2</sup> available from exclusive meson electroproduction data acquired during the 6-GeV era of experiments at Jefferson Laboratory (JLab). These results, combined with achievements in the use of continuum Schwinger function methods (CSMs), offer new opportunities for charting the momentum dependence of the dressed quark mass from results on the  $Q^2$ -evolution of the  $\gamma_v p N^*$  electrocouplings. This mass function is one of the three pillars of EHM and its behavior expresses influences of the other two, *viz.* the running gluon mass and momentum-dependent effective charge. A successful description of the  $\Delta(1232)3/2^+$  and  $N(1440)1/2^+$  electrocouplings has been achieved using CSMs with, in both cases, common momentum-dependent mass functions for the dressed quarks, for the gluons, and the same momentum-dependent strong coupling. The properties of these functions have been inferred from nonperturbative studies of QCD and confirmed, *e.g.*, in the description of nucleon and pion elastic electromagnetic form factors. Parameter-free CSM predictions for the electrocouplings of the  $\Delta(1600)3/2^+$  became available in 2019. The experimental results obtained in the first half of 2022 have confirmed the CSM predictions. We also discuss prospects for these studies during the 12-GeV era at JLab using the CLAS12 detector, with experiments that are currently in progress, and canvass the physics motivation for continued studies in this area with a possible increase of the JLab electron beam energy up to 22 GeV. Such an upgrade would finally enable mapping of the dressed quark mass over the full range of distances (*i.e.* quark momenta) where the dominant part of hadron mass and  $N^*$  structure emerge in the transition from the strongly coupled to perturbative QCD regimes.

**Keywords:** exclusive meson photo- and electroproduction; exclusive reactions with the CLAS and CLAS12 detectors; nucleon resonance photo- and electroexcitation amplitudes; nucleon resonance spectrum and structure; emergence of hadron mass; continuum Schwinger function methods; hadron structure and interactions.



**Citation:** Carman, D.S.; Gothe, R.W.; Mokeev, V.I.; and Roberts, C.D. Nucleon Resonance Electroexcitation and Emergent Hadron Mass. *Particles* **2023**, *1*, 1–23. <https://doi.org/>

Received: 2023 Jan 09

Accepted:

Published:

**Publisher's Note:** MDPI stays neutral with regard to jurisdictional claims in published maps and institutional affiliations.



**Copyright:** © 2023 by the authors. Licensee MDPI, Basel, Switzerland. This article is an open access article distributed under the terms and conditions of the Creative Commons Attribution (CC BY) license (<https://creativecommons.org/licenses/by/4.0/>).

## 1. Introduction

Studies of the strong interaction dynamics that govern the generation of hadron ground and excited states in the regime where the running coupling of quantum chromodynamics (QCD) is large, *i.e.*  $\alpha_s/\pi \approx 1$ , known as the strong QCD (sQCD) regime, represent a crucial challenge in modern hadron physics [1]. The rapid growth of  $\alpha_s$  in the transition

from the perturbative to sQCD domains and particularly its saturation, driven by gluon self-interactions, are predicted by CSMs [2,3] and supported by recent experimental results on the Bjorken sum rule [4]. These trends suggest that the generation of hadron structure in the sQCD regime is defined by emergent degrees of freedom that are related to the partons of QCD's Lagrangian in a non-trivial manner. While this evolution with distance is determined by the QCD Lagrangian, it cannot be analyzed by employing perturbative QCD (pQCD) when  $\alpha_s/\pi$  becomes comparable with unity. The active degrees of freedom seen in hadron structure and their interactions change substantially with distance at the scales where the transition from sQCD to pQCD takes place and the structure of hadron ground and excited states emerges. Understanding how the active degrees of freedom emerge from the QCD Lagrangian and how their interactions evolve with distance requires the development of nonperturbative methods capable of making predictions, both in the meson and baryon sectors, that can be confronted with empirical results on hadron structure extracted using electromagnetic and hadronic probes.

A decade of rapid progress in the development and application of CSMs in hadron physics [5–15], complemented by advances in and results from lattice QCD (lQCD) [16–25], have delivered numerous predictions for properties of mesons and baryons within a common theoretical framework. Studies of hadron structure from data obtained in experiments with electromagnetic probes at JLab [1,26–29], MAMI [30–35], and Babar and Belle [36,37], have provided experimental results that can be confronted with predictions from the QCD-connected approaches to hadron structure. More results are expected from experiments in the ongoing 12-GeV era at JLab [1,38–40] and from planned research programs at the US electron ion collider (EIC) [39,41–43], the electron ion collider in China (EicC) [44,45], and experiments with hadronic probes conducted by the AMBER Collaboration at CERN [46].

Studies of exclusive meson electroproduction in the nucleon resonance excitation region using data from 6-GeV-era experiments at JLab have provided the first and still only available comprehensive information on the electroexcitation amplitudes (*i.e.*  $\gamma_v p N^*$  electrocouplings) of most nucleon excited states in the mass range up to 1.8 GeV for photon virtualities  $Q^2 < 5 \text{ GeV}^2$  (or  $Q^2 < 7.5 \text{ GeV}^2$  for the  $\Delta(1232)3/2^+$  and  $N(1535)1/2^-$ ) [47–51]. Analyses of these results have revealed many facets of strong interactions in the sQCD regime seen in the generation of  $N^*$  states of different quantum numbers with different structural features [28,39,52–61]. These results also enable evaluation of the resonant contributions to inclusive electron scattering observables [62–64], substantially expanding the capability to explore both polarized and unpolarized parton distribution functions (PDFs) of the nucleon for fractional parton light-front momenta close to unity. Analyses of the results on  $\gamma_v p N^*$  electrocouplings within CSMs [1,28,48,59,65–75] have demonstrated a new and promising potential for elucidation of the sQCD dynamics that are responsible for the generation of >98% of the visible mass in the Universe.

Explaining the emergence of hadron mass represents one of the most challenging, open problems in the Standard Model (SM). The emergent nature of hadron mass is made manifest by a comparison between the measured proton and neutron masses and the sum of the current masses of their valence quark constituents. Protons and neutrons are bound systems of three light  $u$ - and  $d$ -quarks. The sum of the current masses of these quarks, which is generated by Higgs couplings into QCD, accounts for less than 2% of the measured nucleon masses (see Table 1). This accounting clearly indicates that the overwhelmingly dominant component of the nucleon mass is created by mechanisms other than those associated with the Higgs boson [8–15].

The past decade of progress using CSMs to study the evolution of hadron structure with distance, maintaining a traceable and often direct connection to the QCD Lagrangian, has conclusively demonstrated that the dominant part of each hadron's mass is generated by strong interactions in the regime of large QCD running coupling [1,8–15,73]. Solving QCD's equations-of-motion for the gluon and quark fields has revealed the emergence of quasiparticles, with the quantum numbers of the Lagrangian partons but carrying

	Proton	Neutron
Measured masses (MeV)	938.2720813 ± 0.0000058	939.5654133 ± 0.0000058
Sum of the current quark masses (MeV)	8.09 <sup>+1.45</sup> <sub>-0.65</sub>	11.50 <sup>+1.45</sup> <sub>-0.60</sub>
Contribution of the current quark masses to the measured nucleon mass (%)	<1.1	<1.4

**Table 1.** Comparison between the measured masses of the proton and neutron,  $m_{p,n}$ , and the sum of the current-quark masses of their three  $u$ - and  $d$ -quark constituents [76]. (Current quark masses listed at a scale of 2 GeV, but the comparison remains qualitatively unchanged if renormalization group invariant current masses are used.)

momentum-dependent masses that are large in the sQCD domain. It is the presence of these quasiparticles within mesons and baryons that explains the greatest part of the visible mass in the Universe.

Herein we describe advances in the exploration of the structure of nucleon excited states, using data from the 6-GeV-era experiments at JLab, and discuss the impact of these results on the understanding of EHM. A successful description of JLab results on the  $\Delta(1232)3/2^+$  and  $N(1440)1/2^+$  electrocouplings has been achieved using CSMs [65, 66,68,69,71]. The CSM calculations are distinguished by (a) having employed common momentum-dependent mass functions for the dressed quarks, whose behavior is intimately connected with the running of the gluon mass and QCD’s effective charge [77] and (b) thereby unifying the description of these electrocouplings with kindred studies of, *inter alia*, nucleon and pion elastic form factors [68,78,79]. Such successes provide a sound foundation for arguments supporting the potential of experimental results on the  $Q^2$ -dependence of nucleon resonance electrocouplings to deliver new information on the running quark mass.

Parameter-free CSM predictions for the  $Q^2$ -evolution of the  $\Delta(1600)3/2^+$  electrocouplings became available in 2019 [74]. At that time, there were no experimental results for the electroexcitation amplitudes of this resonance. Herein, too, we present the first preliminary experimental results on these amplitudes, obtained from analysis of  $\pi^+\pi^-p$  electroproduction data off protons in the  $W$ -range up to 1.7 GeV and  $2 < Q^2/\text{GeV}^2 < 5$  using the JLab-Moscow State University (JM) meson-baryon reaction model [67,80–83]. Comparison between the CSM predictions and these experimental results represents a further sensitive test of the capability for validating the EHM paradigm [8–15].

Our discussion is organized as follows. In Section 2, the basic features of the EHM paradigm are outlined, with special emphasis on the dressed quark and gluon running masses and their evolution in the transition from the weak to strong coupling domains of the strong interaction. We also emphasize the complementarity and critical role of combined studies of both meson and baryon structure in validating any understanding of the generation of the dressed masses of gluon and quark quasiparticles. We outline the analysis framework used for extraction of the  $\gamma_v p N^*$  electrocouplings from data on exclusive meson electroproduction available from experiments during the 6-GeV era at JLab in Section 3. The impact of these results on the understanding of EHM is presented in Section 3.2. In Section 4, plans for future studies and their prospects in ongoing experiments in the 12-GeV era at JLab are highlighted, along with physics motivations for a possible increase of the JLab electron beam energy up to 22 GeV. Such an upgrade would offer the only foreseeable opportunities to explore QCD dynamics in the full range of distances over which the dominant part of hadron mass and structure emerge, particularly reaching, for the first time, into the kinematic region where perturbative and nonperturbative QCD calculations overlap.

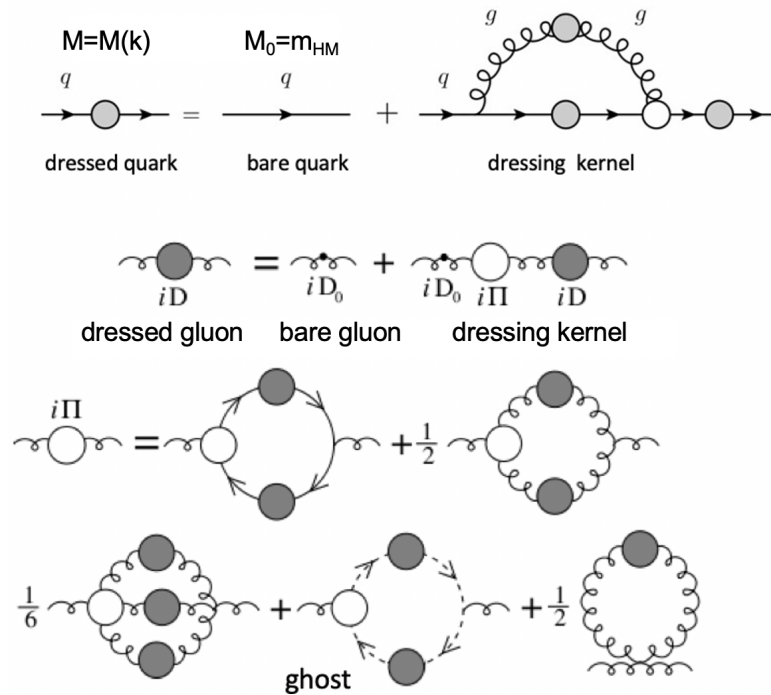


**Figure 1.** Integral equations for the dressed quark and gluon two-point functions [84] (see Section 2.2), drawn in terms of the Feynman diagrams that govern the emergence of gluon and quark quasiparticles from the partons used to express the QCD Lagrangian. These quasiparticles are the active components in hadron structure at low resolving scales. Their parton content is revealed at higher resolutions. (Unbroken lines – quarks; spring-like lines – gluons; short-dashed lines – ghosts; filled circles – dressed propagators; open circles – two-point = self-energies and three/four-point = dressed vertices. The vertices satisfy their own Dyson-Schwinger equations, involving higher  $n$ -point functions [84].)

## 2. Basics for Insight into EHM Using CSMs

The notable progress in developing an understanding of EHM via CSMs has conclusively demonstrated that the dominant part of hadron mass is generated by strong interactions at momentum scales  $k \lesssim 2 \text{ GeV}$ . We now sketch the EHM paradigm and discuss how studies of meson and baryon structure of both ground and excited states offer complementary and crucial information that will enable elucidation of the sQCD dynamics responsible for EHM and its manifold corollaries.

### 2.1. CSMs and the EHM Paradigm

Every scheme proposed for the solution of QCD reveals that the current-quark masses, which are generated by Higgs boson couplings into the Lagrangian, acquire momentum-dependent corrections owing to gluon emission and absorption, as illustrated in Figure 1 (top row). Gluons, too, come to be dressed by the analogous processes shown in Figure 1 (lower rows). Treated in a weak coupling expansion, these “gap equations” generate every diagram in perturbation theory. On the other hand, nonperturbative analyses can reveal emergent features of the strong interaction, such as dynamical chiral symmetry breaking (DCSB) and intimations of confinement [14] (Section 5).

As explained elsewhere [84], the integral equations in Figure 1, and their analogs for higher- $n$ -point functions, can be understood as QCD’s Euler-Lagrange equations, *viz.* QCD’s equations of motion. The solutions of those shown explicitly predict the emergence of gluon and quark quasiparticles, each of which is a superposition of enumerably many gluon and quark (and ghost) partons, is characterized by its own momentum-dependent mass function – see the left panel of Figure 2, and evolves with distance  $1/k$ , where  $k$  is the

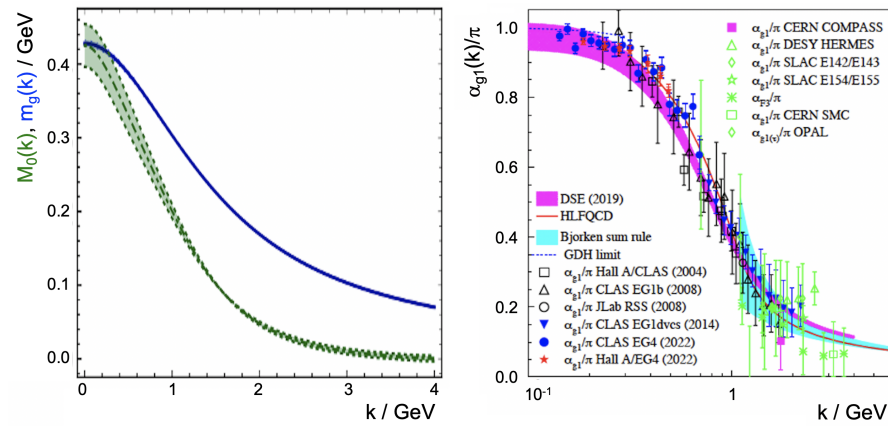


**Figure 2.** (Left): CSM predictions for the momentum dependence of the dressed gluon (blue solid) and quark (green dot-dashed) masses [9–11]. The associated like-colored bands express the uncertainties in the CSM predictions. (N.B. Since the Poincaré-invariant kinetic energy operator for a vector boson has mass-dimension two and that for a spin-half fermion has mass-dimension unity, then for  $m_p^2/k^2 \rightarrow 0$ ,  $M_0(k) \propto 1/k^2$  and  $m_g^2(k) \propto 1/k^2$ , up to  $\ln k^2$  corrections). (Right) CSM prediction [3] (magenta band) for the process-independent QCD running coupling  $\hat{\alpha}_s(Q)$  compared with the empirical results [4] for the process-dependent effective charge defined via the Bjorken sum rule, which is prominent in deep inelastic scattering.

momentum-scale flowing through the diagram, in a well-defined manner that reproduces perturbative results on  $m_p/k \simeq 0$ .

Of primary significance is the dressing of gluons, described by the lower three rows in Figure 1, with effects driven by the three-gluon vertex being most prominent. It was realized long ago [85] that this leads to the emergence of a running gluon mass, like that in Figure 2 (left panel), through the agency of a Schwinger mechanism [86,87] in QCD, the details of which have steadily been unfolded during the past fifteen years [88–92]. This essentially nonperturbative consequence of gauge sector dynamics, revealed in both continuum and lattice-regularized studies of QCD, is the first pillar of EHM.

Capitalizing on such progress in understanding gauge sector dynamics, a unique QCD analog of the Gell-Mann–Low effective charge has been defined and calculated [2,3],  $\hat{\alpha}(k)$ , with the result shown in Figure 2 (right panel). For  $k \gtrsim 2$  GeV, this charge matches the pQCD coupling, but it also supplies an infrared completion of the running coupling, which is free of a Landau pole and saturates to the value  $\hat{\alpha}(k = 0) = 0.97(4)$ . Both these latter features are direct consequences of the emergence of a gluon mass function, whose infrared value is characterized by the renormalization-group-invariant mass-scale  $\hat{m} = 0.43(1)$  GeV  $\approx m_p/2$ . This effective charge is the second pillar of EHM.

As highlighted in Figure 2 (right panel), the pointwise behavior of  $\hat{\alpha}(k)$  is almost identical to that of the process-dependent charge [93,94] defined via the Bjorken sum rule [95,96] for reasons that are explained in Reference [14] (Section 4). The form of  $\hat{\alpha}(k)$  – in particular, its being defined and smooth on the entire domain of spacelike momentum transfers – provides strong support for the conjecture that QCD is a mathematically well-defined quantum gauge field theory. As such, it can serve as a template for extensions of the SM using the notion of compositeness for seemingly pointlike objects.

Turning to the quark gap equation, Figure 1 (top row), and constructing its kernel using the first two pillars of EHM, one obtains a dressed-quark propagator that is characterized by the mass-function shown in Figure 2 (left panel). Critically, for  $k \lesssim 2$  GeV, the behavior of this mass function is practically unchanged in the absence of Higgs boson couplings into QCD, *i.e.*, in the chiral limit. Such an outcome is impossible in pQCD. The emergence of  $M(k)$  is the principal manifestation of DCSB in QCD; and this dressed-quark mass function, again a prediction common to both continuum and lattice-regularized QCD, is the third pillar of EHM.

The appearance of dressed-gluon and -quark quasiparticles following the transition into the domain of sQCD, whose strong mutual- and self-interactions are described by a process-independent momentum-dependent effective charge, form the basis for the EHM paradigm and its explanation of hadron mass and structure. Indeed, it is worth reiterating that the dressed-quark mass function in Figure 2 (left panel) shows how the almost massless current-quark partons, which are the degrees-of-freedom best suited for the description of truly high-energy phenomena, are transmogrified, by a nonperturbative accumulation of interactions, into fully dressed quarks. It is these quark quasiparticles, to which is attached an infrared mass-scale  $M(k \simeq 0) \approx 0.4 \text{ GeV}$ , that provide a link between QCD and the long line of quark potential models developed in the past sixty years [97].

Insofar as the light  $u$ - and  $d$ -quarks are concerned, Higgs boson couplings into QCD are almost entirely irrelevant to the size of their infrared mass, contributing  $< 2\%$  – Reference [11] (Figure 2.5); hence, equally irrelevant to the masses of the nucleon and its excited states. The dominant component of the masses of all light-quark hadrons is that deriving from  $M(k \simeq 0)$ , *viz.* EHM.

Since the quark quasiparticles carry the same quantum numbers as the seed quark-partons, then  $N^*$  electroexcitation processes can be used to chart  $M(k)$  by exploiting the dependence of the associated  $N^*$  electroexcitation amplitudes on the momentum transfer squared. Sketched simply, owing to the quasielastic nature of the transition, the momentum transferred in the process,  $Q$ , is shared equally between the three bound quark quasiparticles in the initial and, subsequently, the final states. This means that the quark mass function is predominantly sampled as  $M(Q/3)$ , because bound-state wave functions are peaked at zero relative momentum. Hence, increasing  $Q$  takes the reaction cross section smoothly from the sQCD (constituent-quark) domain into the pQCD domain. Any Poincaré-invariant, QCD-connected calculational framework can then relate the  $Q^2$ -dependence of the electroexcitation amplitudes to the momentum dependence of the quark mass function and, crucially, when it comes to predictions, vice versa. Examples are provided in References [28,59,65,66,68–71,73,74,98]. Regarding  $M(k)$  in Figure 2, one enters the perturbative domain for  $k \gtrsim 2 \text{ GeV}$ , hence, a comprehensive mapping of the nonperturbative part of the dressed-quark mass requires

$$0 \leq Q^2/\text{GeV}^2 \lesssim 20 - 30. \tag{1}$$

Experiments at JLab during the 6-GeV era provided a beginning, their progeny during the 12-GeV era will extend the map further, but only an upgrade of the JLab accelerator energy to beyond 20 GeV will deliver near exhaustive coverage of the full EHM domain.

### 2.2. Some Highlights from the EHM Experiment-Theory Connection

Charting the dressed-quark mass function using results from hadron structure experiments is a principal goal of modern hadron physics. As always, there are challenges to be overcome, but the potential rewards are great. Empirical verification of the EHM paradigm will pave the way to understanding the origin of the vast bulk of visible mass in the Universe. As illustration, we note that CSMs have supplied a large body of results for meson and baryon structure observables; some examples are shown in Figure 3. Each of these predictions was obtained within a common theoretical framework and expresses different observable consequences of the dressed-gluon and -quark mass functions shown in Figure 2, hence, draws a clear connection between observation and the QCD Lagrangian. Notably, here we have only highlighted results for ground-state hadrons because CSM predictions for the  $\gamma_\nu p N^*$  electrocouplings and their comparison with experimental results are discussed below.

Owing to the pattern of DCSB in QCD, a quark-level Goldberger-Treiman identity [101–105]:

$$f_{\text{NG}} E_{\text{NG}}(k^2) = B(k^2), \tag{2}$$

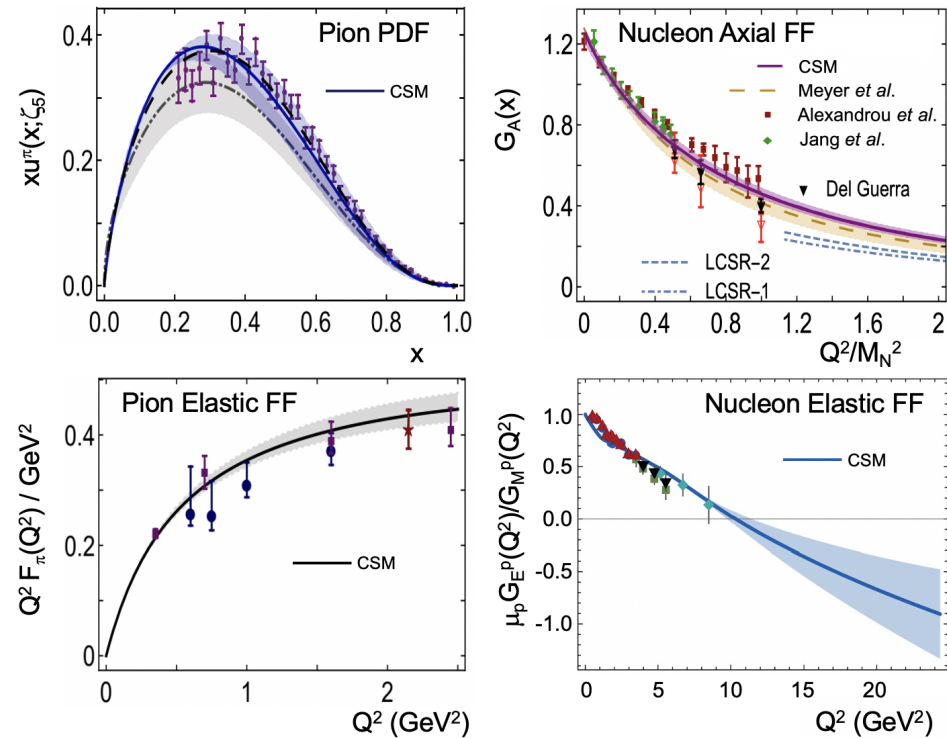


**Figure 3.** CSM predictions for observables of the structure for the ground state hadrons in comparison with experimental results (points with error bars). *Upper left* – pion valence quark PDF [99]; *upper right* – nucleon axial form factor  $G_A$  [100]; *lower-left* – pion elastic form factor [11]; and *lower right* – ratio of nucleon elastic electric and magnetic form factors [79].

relates the leading term in the bound-state amplitude of all Nambu-Goldstone (NG) bosons,  $E_{\text{NG}}(k^2)$ , to the scalar piece of the dressed-quark self energy,  $B(k^2)$ , with the NG boson leptonic decay constant,  $f_{\text{NG}}$ , providing the constant of proportionality. This exact relationship in chiral-limit QCD is Poincaré-invariant, gauge-covariant, and renormalization-scheme independent. It is also the SM’s most fundamental expression of the Nambu-Goldstone theorem [106,107]. Equation 2 explains the seeming dichotomy of massless NG bosons being composites built from massive quark and antiquark quasiparticles; ensuring that all one-body dressing effects that give rise to the quasiparticle masses are cancelled exactly by binding energy with the bound-states, so that they emerge as massless composite objects in the chiral limit [108].

Equation 2 expresses other remarkable facts. It is also a precise statement of equivalence between the pseudoscalar-meson two-body and matter-sector one-body problems in chiral-QCD. These problems are usually considered to be essentially independent. Moreover, it reveals that the cleanest expressions of EHM in the SM are located in the properties of the massless NG bosons. It is worth stressing here that  $\pi$ - and  $K$ -mesons are indistinguishable in the absence of Higgs couplings into QCD. Furthermore, as noted above, Equation 2 entails that they are entirely massless in this limit: the  $\pi$  and  $K$  mesons are the NG bosons that emerge as a consequence of DCSB. At realistic Higgs couplings, however,  $\pi$  and  $K$  observables are windows onto both EHM and its modulation by Higgs boson couplings into QCD.

It is now widely recognized [27,41,43–46] that the quark-level Goldberger-Treiman identity, Equation 2, and its corollaries lift studies of  $\pi$  and  $K$  structure to the highest level of importance. CSM calculations are available for a broad range of such observables; *e.g.*, in a challenge for future high-luminosity, high-energy facilities, a prediction for the elastic electromagnetic pion form factor is now available out to  $Q^2 = 40 \text{ GeV}^2$  – see Reference [41] (Figure 9).

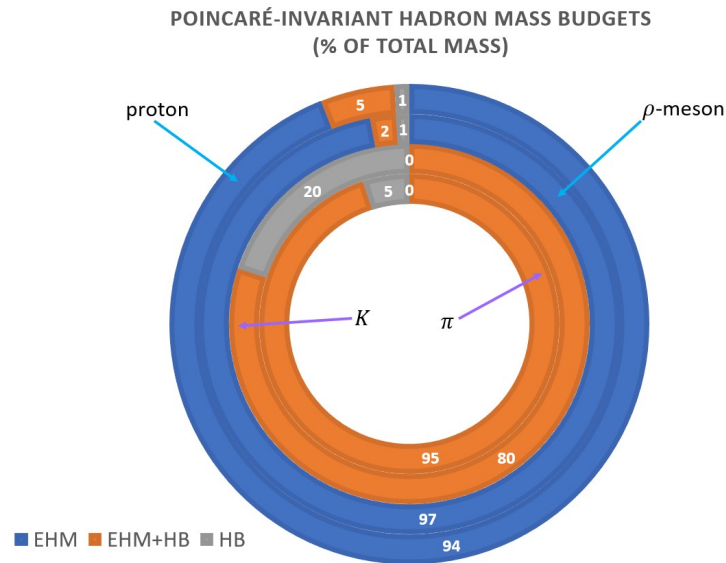


**Figure 4.** Mass budgets for the proton (outermost annulus),  $\rho$ -meson, kaon, and pion (innermost annulus). Each annulus is drawn using a Poincaré-invariant decomposition. The separation is made at a renormalization scale  $\zeta = 2 \text{ GeV}$ , calculated using information from References [109–112].

The peculiar character of NG bosons is further highlighted by the mass budgets drawn in Figure 4, which identify that component of the given hadron’s mass that is generated by (i) EHM; (ii) constructive interference between EHM and the Higgs-boson (HB) mass contribution; and (iii) that part generated solely by the Higgs. The proton annulus depicts information already presented in Table 1 and highlights again that the proton mass owes almost entirely to the mechanisms of EHM. New information is expressed in the second annulus, which is the  $\rho$ -meson mass budget. Plainly, the  $\rho$ -meson and proton mass budgets are qualitatively and semi-quantitatively identical, despite one being a meson and the other a baryon.

The  $\pi$  and  $K$  mass budgets in Figure 4 are completely different. For these (near) NG bosons, there is no pure EHM component – no blue part of the ring – because they are massless in the chiral limit. On the other hand, the HB contribution to the pion mass is commensurate with the kindred component of the proton and  $\rho$ -meson masses. The biggest contribution for the  $\pi$  is EHM+HB interference: the small HB-only contribution is magnified by a huge, latent EHM component. The  $K$ -meson mass budget is similar. However, the larger current-mass of the  $s$ -quark entails that the HB-alone contribution is four-times larger in the  $K$  than in the  $\pi$ , but it is not  $\sim 15$ -times larger, as a simple counting of current-masses would suggest. Evidently, there is some subtlety in EHM+HB interference effects.

This discussion summarizes what others have explained in detail [8–15], namely, that studies of NG bosons on one hand and the nucleon and its excited states on the other provide complementary information about the mechanisms behind EHM: NG bosons reveal much about EHM+HB interference, whereas the other systems are directly and especially sensitive to EHM-only effects. It follows that consistent results on the dressed-quark mass function and, therefrom, indirectly, on the gluon mass and QCD effective coupling, obtained from experimental studies of these complementary systems – NG bosons and the nucleon and its excitations - will shine the brightest light on the many facets and expressions of emergent hadron mass and structure in Nature. Such a broad approach is the best (only?) way to properly verify the EHM paradigm.

### 3. Nucleon Resonance Electrocouplings and their Impact on the Insight into EHM

The contemporary application of CSMs provides a QCD-connected framework that enables development of an understanding of EHM [8–15] from the comparison of theory

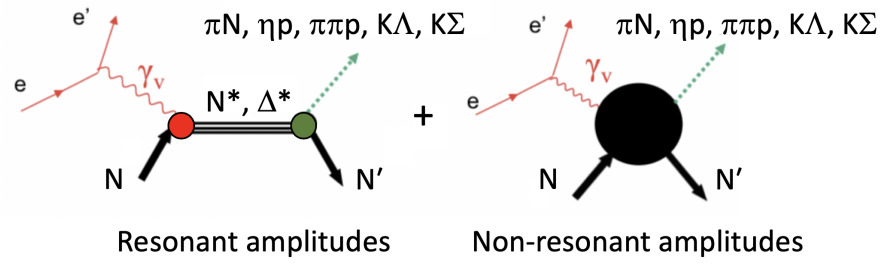


**Figure 5.** Resonant and non-resonant amplitudes contributing to exclusive meson electroproduction channels in the resonance region.

predictions with experimental results on the  $Q^2$ -evolution of nucleon elastic form factors and nucleon resonance electroexcitation amplitudes [48,67,72,75]. In this Section, we provide an overview of experimental  $\gamma_v p N^*$  results where comparisons with CSM predictions exist.

### 3.1. Extraction of Electrocouplings from Exclusive Meson Electroproduction Data

Nucleon resonance electroexcitations can be fully described in terms of three electroexcitation amplitudes or  $\gamma_v p N^*$  electrocouplings.  $A_{1/2}(Q^2)$  and  $A_{3/2}(Q^2)$  describe resonance production in the process  $\gamma_v p \rightarrow N^*, \Delta^*$  by transversely polarized photons of helicity  $+1$  ( $-1$ ) and target proton helicities  $\pm 1/2$  ( $\mp 1/2$ ) in the center-of-mass (CM) frame, with the resonance spin projection, directed parallel (antiparallel) to the  $\gamma_v$  momentum, equal to  $1/2$  ( $-1/2$ ) and  $3/2$  ( $+3/2$ ), respectively. The resonance electroexcitation amplitudes of the other (flipped) helicities of the initial photon and target proton and the resonance spin projections are related by parity transformations.  $S_{1/2}(Q^2)$  describes accordingly the resonance electroexcitation by a longitudinal virtual photon of zero helicity and target proton helicities  $\pm 1/2$ , with the absolute value of the resonance spin projection equal to  $1/2$  [49]. Since parity is conserved in both electromagnetic and strong interactions, the  $A_{1/2}(Q^2)$ ,  $A_{3/2}(Q^2)$ , and  $S_{1/2}(Q^2)$  electrocouplings describe all possible  $N^*$  electroexcitation amplitudes. These electrocouplings are unambiguously determined through their relation with the resonance electromagnetic decay widths,  $\Gamma_\gamma^T$  and  $\Gamma_\gamma^L$ , to the final state for transversely and longitudinally polarized photons:

$$\Gamma_\gamma^T(W = M_r, Q^2) = \frac{q_{\gamma,r}^2(Q^2)}{\pi} \frac{2M_N}{(2J_r + 1)M_r} \left( |A_{1/2}(Q^2)|^2 + |A_{3/2}(Q^2)|^2 \right), \quad (3a)$$

$$\Gamma_\gamma^L(W = M_r, Q^2) = \frac{q_{\gamma,r}^2(Q^2)}{\pi} \frac{2M_N}{(2J_r + 1)M_r} |S_{1/2}(Q^2)|^2, \quad (3b)$$

with  $q_{\gamma,r} = q_\gamma|_{W=M_r}$ , the absolute value of the  $\gamma_v$  three momentum at the resonance point,  $M_r$  and  $J_r$  being the resonance mass and spin, respectively, and  $M_N$  the nucleon mass.  $W$  is the sum of the energies of the  $\gamma_v$  and target proton in their CM frame.

Alternatively, the resonance electroexcitation can be described by three transition form factors,  $G_{1,2,3}(Q^2)$  or  $G_{M,E,C}^*(Q^2)$ , which represent Lorentz invariant functions in the most general expressions for the  $N \rightarrow N^*$  electromagnetic transition currents. For spin  $1/2$  resonances, the  $F_{1,2}^*(Q^2)$  Dirac and Pauli transition form factors can also be used instead of  $G_{1,2,3}(Q^2)$  or  $G_{M,E,C}^*(Q^2)$ . The description of resonance electroexcitation in terms of the electrocouplings and the electromagnetic transition form factors is completely equivalent, since they are unambiguously related, as described in References [49,113].

The  $\gamma_v p N^*$  electrocouplings have been determined from data on exclusive meson electroproduction for most relevant channels in the resonance excitation region, including  $\pi N$ ,  $\eta p$ , and  $\pi^+ \pi^- p$ . The extractions for  $KY$  channels are still awaiting the development of a reaction model capable of describing electroproduction observables with accuracy

Meson electroproduction channels	Excited proton states	$Q^2$ ranges for extracted $\gamma_v p N^*$ electrocouplings, GeV <sup>2</sup>
$\pi^0 p, \pi^+ n$	$\Delta(1232)3/2^+$ $N(1440)1/2^+, N(1520)3/2^-$ $N(1535)1/2^-$	0.16-6 0.30-4.16 0.30-4.16
$\pi^+ n$	$N(1675)5/2^-, N(1680)5/2^+$ $N(1710)1/2^+$	1.6-4.5
$\eta p$	$N(1535)1/2^-$	0.2-2.9
$\pi^+ \pi^- p$	$N(1440)1/2^+, N(1520)3/2^-$ $\Delta(1600)3/2^+, \Delta(1620)1/2^-$ $N(1650)1/2^-, N(1680)5/2^+,$ $\Delta(1700)3/2^-$ $N(1720)3/2^+, N'(1720)3/2^+$	0.25-1.50 2.0-5.0 0.50-1.50 0.50-1.50

**Table 2.** Summary of the results for the  $\gamma_v p N^*$  electrocouplings from the  $\pi N$ ,  $\eta p$ , and  $\pi^+ \pi^- p$  electroproduction channels measured with the CLAS detector in Hall B at JLab.

sufficient for the reliable separation of the resonant/non-resonant contributions [114,115]. The full amplitude for any exclusive electroproduction channel can be described as the coherent sum of the  $N^*$  electroexcitations in the  $s$ -channel for the virtual photon-proton interaction and a complex set of non-resonant mechanisms, as depicted in Figure 5. The electrocouplings determined from all exclusive meson electroproduction channels should be the same for a given  $N^*$  state, since they should be independent of their hadronic decays, while the non-resonant amplitudes are different for each exclusive meson electroproduction channel. Hence consistent results on the  $Q^2$ -evolution of the electrocouplings extracted from different decay channels enable evaluation of the systematic uncertainties related to the use of the reaction models employed in the analysis.

Systematic studies of  $N^*$  electroexcitation from the data became feasible only after experiments during the 6-GeV era with the CLAS detector in Hall B at JLab. This detector has collected the dominant part of available world data on most single- and multi-meson electroproduction channels off protons in the resonance region for  $Q^2$  up to 5 GeV<sup>2</sup> [47–49, 72,75]. The data are stored in the CLAS Physics Database [116,117]. For the first time, a large body of data ( $\approx$  150k points) on differential cross sections and polarization asymmetries has become available with nearly complete coverage for the final state hadron CM emission angle, which is important for the reliable extraction of electrocouplings.

Several reaction models have been developed for the extraction of electrocouplings from independent studies of the  $\pi N$  [118–127],  $\eta N$  [127–131], and  $\pi^+ \pi^- p$  [67,80–83] electroproduction channels off protons. Coupled-channel approaches [132–134] are making steady progress toward determining the electrocouplings from global multichannel analyses of the combined data for exclusive meson photo-, electro-, and hadroproduction. These analyses will allow for the explicit incorporation of final state interactions between all open channels for the strong interactions between the final state hadrons. Application of such advanced coupled-channel approaches will also enable the restrictions imposed on the photo-, electro-, and hadroproduction amplitudes by the general unitarity condition to be consistently taken into account. An important extension of the database on the exclusive meson hadroproduction channels is expected from the JPARC experimental program [135,136]. These data will be of particular importance in extending the extraction of the electrocouplings within global multichannel analyses toward  $W > 1.6$  GeV.

Analyses of CLAS results from the exclusive  $\pi N$ ,  $\eta p$ , and  $\pi^+ \pi^- p$  electroproduction channels have provided the first and still only available comprehensive information on the electrocouplings of most excited proton states in the range of  $W < 1.8$  GeV and  $Q^2 < 5$  GeV<sup>2</sup> (see Table 2). The experiments of the 6-GeV era in Halls A/C at JLab further

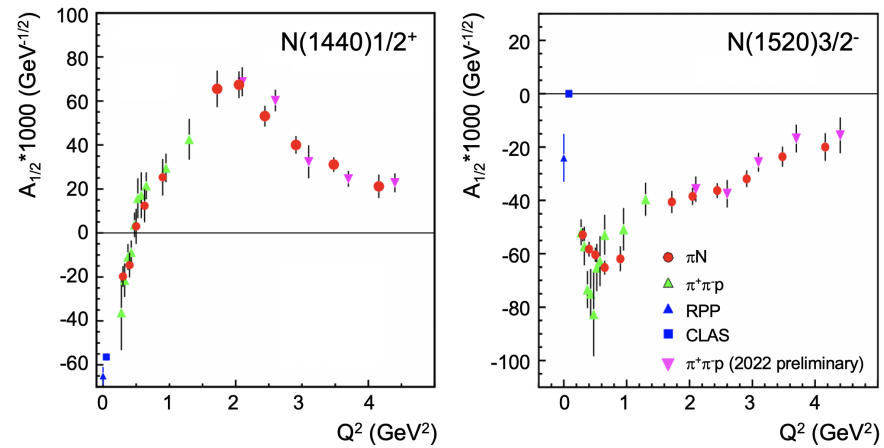


**Figure 6.**  $N(1440)1/2^+$  and  $N(1520)3/2^-$  electrocouplings extracted from the  $\pi N$  [124,137] and  $\pi^+ \pi^- p$  [67,83,138,139] electroproduction channels. The photocouplings from the Review of Particle Properties (RPP) [112] and from Reference [140] are shown by the blue squares and triangles, respectively.

extended this information, providing  $\Delta(1232)3/2^+$  and  $N(1535)1/2^-$  electrocouplings for  $Q^2 < 7 \text{ GeV}^2$  [50,51].

As representative examples, the transverse  $A_{1/2}(Q^2)$  electrocouplings versus  $Q^2$  for the  $N(1440)1/2^+$  and  $N(1520)3/2^-$ , obtained from independent studies of the  $\pi N$  [124,137] and  $\pi^+ \pi^- p$  [67,83] channels, are shown in Figure 6. The electrocouplings inferred from data on the two major  $\pi N$  and  $\pi^+ \pi^- p$  electroproduction channels, with different non-resonant contributions, are consistent. This success, reproduced for all available electrocouplings and reaction channels (see Table 2), has demonstrated the capabilities of these reaction models, developed by the CLAS Collaboration, for the credible extraction of the  $\gamma_v p N^*$  electrocouplings from independent studies of different electroproduction channels.

### 3.2. Insights into the Dressed-Quark Mass Function from the $\gamma_v p N^*$ Electrocouplings

Results on the  $Q^2$  evolution of the  $\gamma_v p N^*$  electrocouplings available from experiments performed during the 6-GeV era at JLab have already had a substantial impact on understanding the sQCD dynamics responsible for the saturation of the running coupling  $\alpha_s$ ,  $N^*$  structure, and the generation of a significant portion of hadron mass [1,28]. Analyses of these results have revealed  $N^*$  structure to emerge from a complex interplay between the inner core of three dressed quarks and an outer meson-baryon cloud [1,28,67,141]. Successful descriptions of the data on the dominant  $N \rightarrow \Delta(1232)3/2^+$  magnetic transition form factor [50,137] and the electrocouplings of the  $N(1440)1/2^+$  [75,124,137] have been achieved using CSMs [65,66,68,69] for  $Q^2 > 1.0 \text{ GeV}^2$  and  $Q^2 > 2.0 \text{ GeV}^2$ , respectively (see Figure 7). These  $Q^2$  ranges correspond to the distance scales where contributions from the quark core to the resonance structure come to dominate. Since the CSM evaluations account for the contributions from only the quark core, they can only reasonably be confronted with experimental results in the higher- $Q^2$  range, where the quark core contributions to  $N^*$  structure dominate over those from the meson-baryon cloud.

The sensitivity of the electroexcitation amplitudes to the momentum-dependence of the quark mass function is dramatically illustrated by Figure 7, which deliberately shows results obtained with  $M(k) = \text{constant}$  [65,66] and  $M(k)$  from Figure 2 [68,69]. The  $M(k) = 0.36 \text{ GeV}$  results were computed first in order to provide a “straw-man” benchmark against which the subsequent realistic  $M(k)$  results could be contrasted. The constant-mass results (dotted red curves in Figure 7) overestimate the data on the  $N \rightarrow \Delta$  magnetic transition form factor for  $Q^2 \gtrsim 1 \text{ GeV}^2$ . The discrepancy increases with  $Q^2$ , approaching an order of magnitude difference in the ratio at  $5 \text{ GeV}^2$ . Moreover, whilst reproducing the

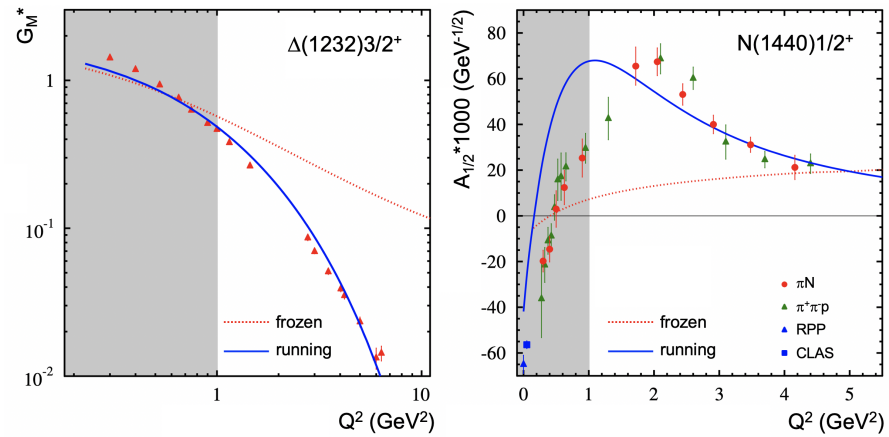


**Figure 7.** Description of the results for the  $N \rightarrow \Delta$  magnetic transition form factor  $G_M^*$  (left) and the electrocoupling amplitude  $A_{1/2}$  for the  $N \rightarrow N(1440)1/2^+$  (right) achieved using CSMs [65,66,68,69]. Results obtained with a momentum-independent (frozen) dressed-quark mass [65,66] (dotted red curves) are compared with QCD-kindred results (solid blue curves) obtained with the momentum-dependent quark mass function in Figure 2. The electrocoupling data were taken from References [50, 122,124] –  $\pi N$  electroproduction; and References [67,83,138,139] –  $\pi^+ \pi^- p$  electroproduction. The photocouplings for the  $N(1440)1/2^+$  are from the RPP [112] and from Reference [140] – blue square and triangle, respectively. The ranges of  $Q^2$  where the contributions from the meson-baryon cloud remain substantial are highlighted in gray.

zero in  $A_{1/2}$  for the  $N(1440)1/2^+$ , the frozen mass result is otherwise incompatible with the data. Plainly, therefore, the data speak against dressed-quarks with a frozen mass. On the other hand, in both cases, the transition form factors are well described by an internally consistent CSM calculation built upon the mass function in Figure 2 – see the solid blue curves in Figure 7. These observations confirm the statements made above, *viz.* nucleon resonance electroexcitation amplitudes are keenly sensitive to the form of the running quark mass. Moreover, the agreement with the larger- $Q^2$  data clearly points to a dominance of the dressed-quark core of the nucleon resonances in the associated domains.

It is worth stressing that the CSM results for the  $\Delta(1232)3/2^+$  and  $N(1440)1/2^+$  electroexcitation amplitudes were obtained using the same dressed-quark mass function, *i.e.*,  $M(k)$  in Figure 2: indeed, the theory analyses of both transitions used precisely the same framework. The common quark mass function matches that obtained by solving the quark gap equation in Figure 1 with a kernel built from the best available inputs for [77]: the gluon two-point function, running coupling, and dressed gluon-quark vertex. Moreover, the same mass function was also used in the successful description of the experimental results on nucleon elastic electromagnetic form factors [68,79], and axial and pseudoscalar form factors [100,142]. Such a mass function is also a key element in an *ab initio* treatment of pion electromagnetic elastic and transition form factors [78,143,144].

These CSM results for meson and baryon properties, both ground and excited states, are part of a large body of mutually consistent predictions. Their success in describing and explaining data relating to such a diverse array of systems provides strong evidence in support of the position that dressed-quarks, with dynamically generated running masses, are the appropriate degrees-of-freedom for use in the description of the mass and structure of all hadrons. This realization is one of the most important achievements of hadron physics during the past decade, and it was only accomplished through numerous synergistic interactions between experiment, phenomenology, and theory.

### 3.3. Novel Tests of CSM Predictions

In 2019, CSM predictions became available for the electrocouplings of the  $\Delta(1600)3/2^+$  [74]. This baryon may be interpreted in quantum field theory as a state with aspects

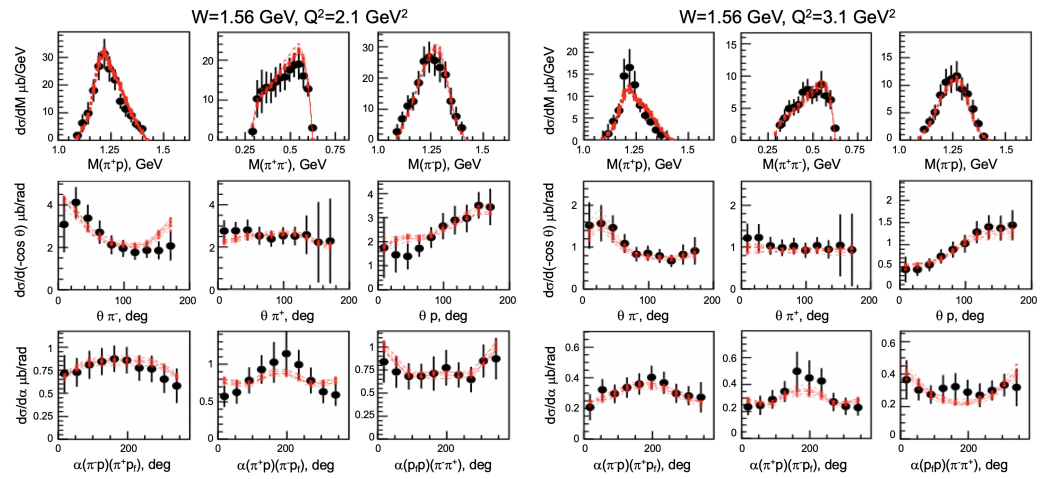


**Figure 8.** Regarding extraction of  $\Delta(1600)3/2^+$  electrocouplings, representative examples of the nine independent one-fold differential cross sections available from the  $\pi^+\pi^-p$  measurements with CLAS [146,147] at two different  $Q^2$  values, along with the data fits within the data-driven meson-baryon JM reaction model [75,82,83].

of the character of a first radial excitation of the  $\Delta(1232)3/2^+$  [56,61], for which CSM electrocoupling results became available earlier [68] and are discussed above.

No relevant experimental results were available when the  $\Delta(1600)3/2^+$  predictions were made. The first (and still preliminary) results for the  $\Delta(1600)3/2^+$  electrocouplings only became available in the first half of 2022 [138,139,145]. They were extracted from the analysis of  $\pi^+\pi^-p$  electroproduction off protons measured with the CLAS detector [146, 147] for  $W$  from 1.4–2.1 GeV and  $Q^2$  from 2–5 GeV<sup>2</sup>. Nine independent one-fold differential cross sections were analyzed in each  $(W, Q^2)$  bin. The final-state hadron kinematics is fully determined by the five-fold differential cross sections. The one-fold differential cross sections were obtained by integrating the five-fold differential cross sections over different sets of four kinematic variables [82,83]. For extraction of the electrocouplings, it was necessary to fit the data for the three invariant mass distributions for the different pairs of final-state hadrons, the distributions of the final-state hadrons over the CM polar angles  $\theta_i$  ( $i = \pi^+, \pi^-, p_f$ ), and the distributions over the three CM angles  $\alpha_{[i],[j]}$  between the two planes: one of which [ $i$ ] is the reaction plane defined by the three-momentum of the  $\gamma_v$  and one of the final state hadrons, and the second [ $j$ ] is determined by the three-momenta of the other two final-state hadrons for the three possible choices of the hadron pairs. Representative examples of the data measured are shown in Figure 8 at the  $W$ -bins closest to the Breit-Wigner mass of the  $\Delta(1600)3/2^+$  and in different bins of  $Q^2$ .

The  $N^*$  electrocouplings on the domain  $W < 1.65$  GeV were obtained from the fit of the differential  $\pi^+\pi^-p$  photo- and electroproduction cross sections carried out within the framework of the data-driven JM meson-baryon reaction model [67,80–83]. This model has been developed by the CLAS Collaboration for the extraction of nucleon resonance electrocouplings and their partial hadronic decay widths to the  $\pi\Delta$  and  $\rho p$  final states. Within the JM model, the full 3-body  $\pi^+\pi^-p$  electroproduction amplitude includes the contributions from  $\pi^-\Delta^{++}$ ,  $\rho p$ ,  $\pi^+\Delta^0$ ,  $\pi^+N(1520)3/2^-$ , and  $\pi^+N(1685)5/2^+$ , with subsequent decays of the unstable intermediate hadrons. It also contains direct  $2\pi$  photo-/electroproduction processes, where the final  $\pi^+\pi^-p$  state is created without the generation of unstable intermediate hadrons. Here the nucleon resonances contribute to the  $\pi^-\Delta^{++}$ ,  $\pi^+\Delta^0$ , and  $\rho p$  channels.

Modeling of the non-resonant contributions is described in References [80–83]. For the resonant contributions, the JM model includes all four-star Particle Data Group (PDG)  $N^*$  states with observed decays to  $\pi\pi N$ , as well as the new  $N'(1720)3/2^+$  resonance [148, 149] observed in the combined analysis of  $\pi^+\pi^-p$  photo- and electroproduction data.

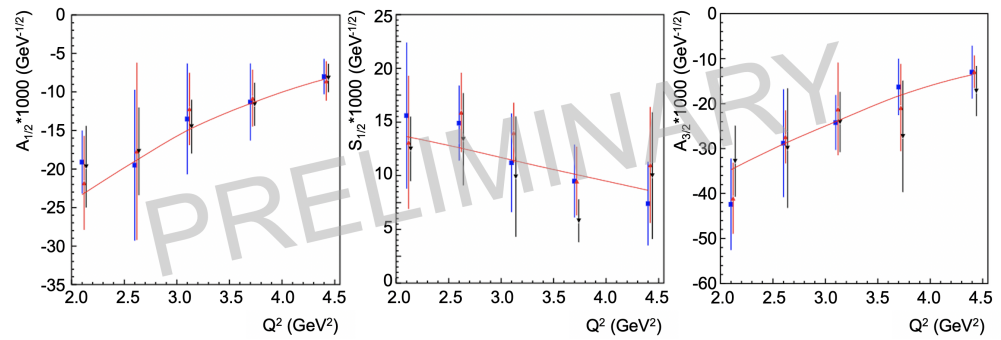


**Figure 9.**  $\Delta(1600)3/2^+$  electrocouplings with their assigned uncertainties, determined from independent analysis of the  $\pi^+\pi^-p$  differential cross sections in three overlapping  $W$  intervals: 1.46–1.56 GeV (filled blue squares), 1.51–1.61 GeV (filled red triangles), and 1.56–1.66 GeV (filled black triangles) [138,139,145]. CSM predictions [74] are drawn as solid red curves.

The resonant amplitudes are described within the unitarized Breit-Wigner *ansatz* [83], thereby ensuring consistency with restrictions imposed by the general unitarity condition. The JM model offers a good description of the  $\pi^+\pi^-p$  differential cross sections in the entire kinematic area covered by the data at  $W < 2.1$  GeV and  $Q^2 < 5$  GeV<sup>2</sup>. All of the electrocouplings extracted from the  $\pi^+\pi^-p$  data (published, in part, also in the PDG) have been determined using the JM reaction model.

In the analyses of the  $\pi^+\pi^-p$  data [146,147], the following quantities were varied: the  $\gamma_0 p N^*$  electrocouplings for the resonances in the mass range  $< 1.75$  GeV, their partial hadronic decay widths into the  $\pi\Delta$  and  $\rho p$  final states, their total decay widths, and the non-resonant parameters of the JM model. For each trial attempt at a data description,  $\chi^2/d.p.$  ( $d.p.$  = data point) was computed by the comparison between the measured and computed nine one-fold differential cross sections. In the fits, the computed cross sections closest to the data were selected by requiring  $\chi^2/d.p.$  to be below a predetermined threshold, ensuring that the spread of the selected phenomenological fit cross sections lies within the data uncertainties for most experimental data points. Representative examples are shown by the family of curves in Figure 8.

The electrocouplings for the computed cross sections selected from the data fits were averaged together and their means were treated as the experimental value. The RMS width of the determined electrocouplings was assigned as the corresponding uncertainty. The preliminary results of this extraction for the  $\Delta(1600)3/2^+$  [138,139,145] are shown in Figure 9, wherein they are compared with the CSM predictions obtained three years earlier [74]. These results were determined for overlapping  $W$ -intervals: 1.46–1.56 GeV, 1.51–1.61 GeV, and 1.56–1.66 GeV for  $Q^2$  from 2–5 GeV<sup>2</sup>. The non-resonant contributions in these  $W$ -intervals are different. The electrocouplings determined from the independent fits of the data within the three  $W$ -intervals are consistent, establishing their reliability and confirming the CSM predictions. This success has markedly strengthened the body of evidence that indicates that detailed information can be obtained on the momentum dependence of the dressed-quark mass function from sound data on  $N^*$  electroproduction, and, therefrom, deep insights into the character of EHM in the SM.

#### 4. Studies of $N^*$ Structure in Experiments with CLAS12 and Beyond

Most results on the  $N^*$  electrocouplings have been obtained for  $Q^2 < 5$  GeV<sup>2</sup>. Detailed comparison of these results with the CSM predictions allow for exploration of the quark mass function within the range of quark momenta  $< 0.75$  GeV, assuming equal sharing of the virtual-photon momentum-transfer between the three dressed quarks in the transition between the ground and excited nucleon states. The results on the resonance electrocouplings in this range of quark momentum, shown in Figure 10 (top), cover distances over which less than 30% of hadron mass is generated [9,10].

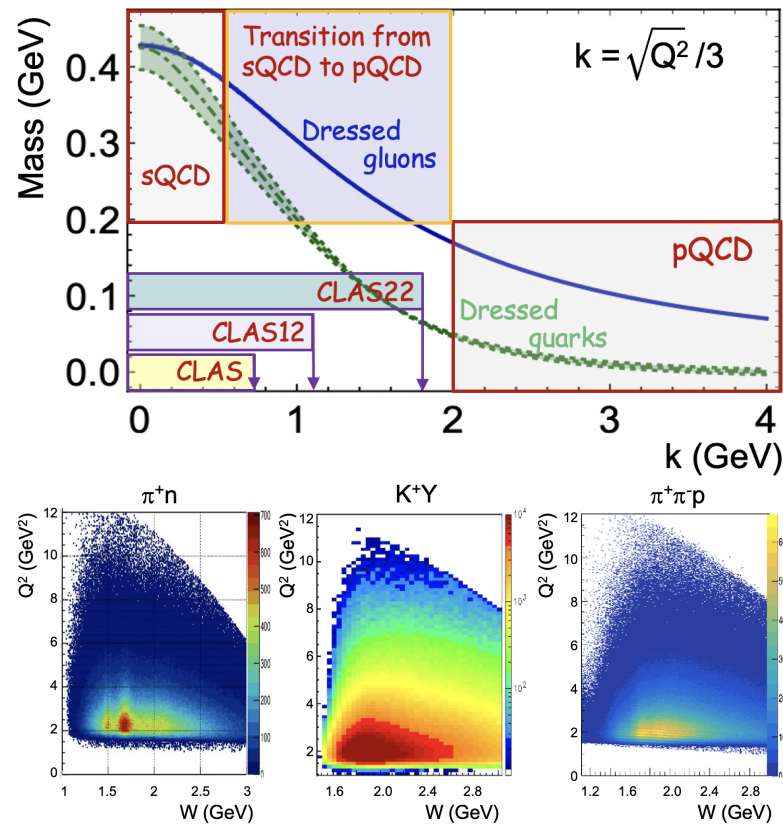


**Figure 10.** (Top) Momentum ranges accessible in the exploration of the momentum dependence of the dressed quark mass function using results on the  $Q^2$  evolution of  $\gamma_v p N^*$  electrocouplings. The range of  $k$  covered by available data is mostly from experiments with CLAS, shown in yellow. The expected reach of CLAS12 experiments is shown in purple and that achievable after a proposed increase of the JLab beam energy to 22 GeV in cyan. (Bottom) Yields of representative exclusive meson electroproduction channels available from the experiments with the CLAS12 detector.

In the northern spring of 2018, after completion of the 12-GeV-upgrade project, measurements with the CLAS12 detector in Hall B at JLab commenced [47,48,150]. Currently, CLAS12 is the only facility in the world capable of exploring exclusive meson electroproduction in the resonance region, exploiting the highest  $Q^2$  ever achieved for these processes. Ongoing experiments with electron beam energies up to 11 GeV with CLAS12 offer a unique opportunity to obtain information on the electrocouplings of the most prominent  $N^*$  states in the mass range up to 2.5 GeV at  $Q^2$  up to 10 GeV<sup>2</sup> from the exclusive  $\pi N$ ,  $KY$  ( $Y=\Lambda$  or  $\Sigma$ ),  $K^*Y$ ,  $KY^*$ , and  $\pi^+\pi^-p$  channels [114,115,151–153].  $Q^2$  versus  $W$  event distributions for these exclusive reaction channels measured with CLAS12 at a beam energy of  $\sim 11$  GeV are shown in Figure 10 (bottom). The first results from the CLAS12  $N^*$  program (at lower beam energies of 6.5/7.5 GeV) have recently been published on the beam-recoil hyperon transferred polarization in  $K^+Y$  electroproduction [154]. The increase in the  $Q^2$ -coverage for results on the electrocouplings from CLAS12 will enable exploration of the dressed quark mass within the range of quark momenta where roughly 50% of hadron mass is expected to be generated (see Figure 10 (top)).

In order to solve the challenging SM problems relating to EHM, the dressed quark mass function should be charted over the entire quark momentum range up to  $\approx 2$  GeV. This is the domain of transition from strong to perturbative QCD (see Figure 10 (top)) and where dressed quarks and gluons become the relevant degrees-of-freedom as  $\alpha_s/\pi \rightarrow 1$ , approaching the sQCD saturation regime (see Figure 2). This objective requires a further extension of the electrocoupling measurements up to  $Q^2 \approx 30$  GeV<sup>2</sup>. Discussions and planning are currently underway, focusing on an energy-increase of the JLab accelerator to

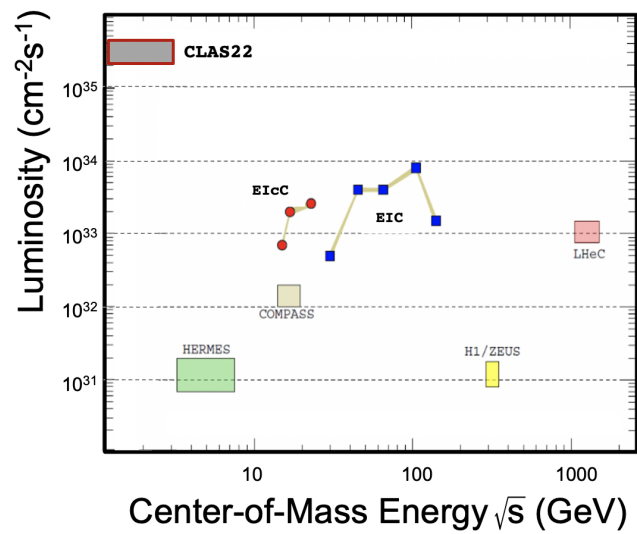


**Figure 11.** Luminosity versus CM energy in lepton-proton collisions for existing and foreseeable facilities capable of exploring hadron structure in measurements with large-acceptance detectors.

a beam energy of 22 GeV, after the completion of the experiments planned for the 12-GeV program. Initial simulations of  $\pi N$ ,  $KY$ , and  $\pi^+ \pi^- p$  electroproduction at 22 GeV using the existing CLAS12 detector at a luminosity up to  $(2 - 5) \times 10^{35} \text{ cm}^{-2}\text{s}^{-1}$  have shown that a measurement program of 1-2 years duration would enable measurements of sufficient statistical accuracy to determine the  $\gamma_v p N^*$  electrocouplings of the most prominent  $N^*$  states over this full kinematic range.

Figure 11 shows the luminosity versus CM energy in lepton-proton collisions for existing and foreseeable facilities capable of exploring hadron structure in measurements with large-acceptance detectors. The luminosity requirements for the extraction of electrocouplings within the  $Q^2$  range 10-30  $\text{GeV}^2$  exceed by more than an order-of-magnitude the maximum luminosity planned for experiments with the EIC [42] and EicC [45]  $ep$  colliders and even more for other facilities. The combination of a high duty-factor JLab electron beam at 22 GeV with the capacity to measure exclusive electroproduction reactions at luminosities of  $(2 - 5) \times 10^{35} \text{ cm}^{-2}\text{s}^{-1}$  using a large-acceptance detector, would make a 22 GeV JLab unique. It would be the only facility in the world able to explore the evolution of hadron structure over essentially the full range of distances where the transition from strong-coupling QCD to the weak-field domain is expected to occur.

The increase of the JLab energy to 22 GeV, pushing the current CLAS12 detector capabilities to measure exclusive electroproduction to the highest possible luminosity and extending the available reaction models used for the extraction of the electrocouplings, will offer the only foreseeable opportunity to explore how the dominant part of hadron mass (up to 85%) and  $N^*$  structure emerge from QCD. This would make an energy-upgraded JLab at 22 GeV the ultimate QCD-facility at the luminosity frontier.

### 5. Conclusions and Outlook

Baryons are the most fundamental three-body systems in Nature. If we do not understand how QCD generates these bound states of three dressed quarks, then our understanding of Nature is incomplete. Remarkable progress has been achieved in recent decades through the studies of the structure of the ground and excited nucleon states in experiments at JLab during the 6-GeV era [1,28,47–49,72,155,156]. These experiments have provided a large array of new opportunities for QCD-connected hadron structure theory by opening a door to the exploration of many hitherto unseen facets of the strong interaction in the regime of large running coupling, *i.e.*,  $\alpha_s/\pi \gtrsim 0.2$ , by providing the results on the  $\gamma_v p N^*$

electrocouplings for numerous  $N^*$  states, with different quantum numbers and structural features.

High-quality meson electroproduction data from the 6-GeV era at JLab have enabled determination of the electrocouplings of most nucleon resonances in the mass range up to 1.8 GeV for  $Q^2 < 5 \text{ GeV}^2$  (up to  $7.5 \text{ GeV}^2$  for the  $\Delta(1232)3/2^+$  and  $N(1535)1/2^-$ ). Consistent results on the  $Q^2$  evolution of these electrocouplings from analyses of  $\pi^+n$ ,  $\pi^0p$ ,  $\eta p$ , and  $\pi^+\pi^-p$  electroproduction have demonstrated the capability of the reaction models employed to extract the electrocouplings in independent studies of all of these different exclusive channels. Above, we have sketched how comparisons between the experimental results on the  $Q^2$  evolution of the  $\gamma_v p N^*$  electroexcitation amplitudes and QCD-connected theory have vastly improved our understanding of the momentum dependence of the dressed quark mass function, which is one of the three pillars of EHM. The remaining two pillars are the running gluon mass and the QCD effective charge, and these entities, too, are constrained by the electroexcitation data.

A good description of the  $\Delta(1232)3/2^+$  and  $N(1440)1/2^+$  electrocouplings has been achieved using CSMs in the full range of photon virtualities where the structure of these excited states is principally determined by contributions from a core of three dressed quarks. The successful description of the electrocouplings for nucleon resonances of different structure, spin+isospin flip for the  $\Delta(1232)3/2^+$  and the first radial excitation of three dressed quarks for the  $N(1440)1/2^+$ , was achieved with the same dressed quark mass function. This mass function is determined by QCD dynamics, and such a running mass has also been used in the successful description of data on elastic electromagnetic nucleon and pion form factors, as well as for the description of the nucleon axial form factor  $G_A$ . In thereby arriving at a unification of diverse observables, one obtains compelling evidence in support of the momentum dependence of the dressed quark mass used to describe the results on the  $Q^2$  evolution of the electrocouplings.

This impressive hadron physics achievement in the past decade was accomplished through synergistic efforts between experiment, phenomenology, and QCD-connected hadron structure theory. In 2019 CSMs provided parameter-free predictions for the electrocouplings of the  $\Delta(1600)3/2^+$ . There were no experimental results available at that time. The first, preliminary results on the  $\Delta(1600)3/2^+$  electrocouplings extracted from the data on  $\pi^+\pi^-p$  electroproduction are reported herein. They have strikingly confirmed the CSM predictions.

Most results for the  $\gamma_v p N^*$  electrocouplings are currently available for  $Q^2 < 5 \text{ GeV}^2$ , allowing for the exploration of the dressed quark mass within the limited range of quark momenta where less than 30% of hadron mass is expected to be generated. Experiments on exclusive meson electroproduction in the resonance region are now in progress with the CLAS12 detector in Hall B at JLab, following completion of the 12-GeV-upgrade project. CLAS12 is the only facility in the world capable of obtaining the electrocouplings of all prominent  $N^*$  states in the still unexplored  $Q^2$  range from 5–10  $\text{GeV}^2$  from measurements of  $\pi N$ ,  $\eta p$ ,  $\pi^+\pi^-p$ , and  $KY$  electroproduction. These data will probe the dressed quark mass function at quark momenta up to  $\approx 1.1 \text{ GeV}$ , a domain where up to 50% of hadron mass is generated.

In order to solve the problem of EHM, a key challenge within the SM, the dressed quark mass function should be mapped over the entire range of quark momenta up to  $\approx 2 \text{ GeV}$ , where the transition from strong to perturbative QCD takes place and where gluon and quark quasiparticles with dynamically generated running masses emerge as  $\alpha_s/\pi \rightarrow 1$ . This requires an extension of existing and anticipated data so that it covers the  $Q^2$ -domain from 10–30  $\text{GeV}^2$ . Explorations of the possibility to increase the JLab beam energy to 22 GeV are now in progress. Such a machine would enable coverage over the desired  $Q^2$  range within the region of  $W < 2.5 \text{ GeV}$ . Simulations with the existing CLAS12 detector configuration for the exclusive  $\pi N$ ,  $KY$ , and  $\pi^+\pi^-p$  electroproduction channels at 22 GeV beam energy and a luminosity of  $(2 - 5) \times 10^{35} \text{ cm}^{-2}\text{s}^{-1}$  show that, with beam-times of 1-2 years, differential cross section and polarization asymmetry measurements of sufficient

statistical precision can be achieved to extract electrocouplings of all prominent resonances up to 30 GeV<sup>2</sup>. Both the EIC and EicC *ep* colliders would need much higher and foreseeably unreachable luminosities than currently envisaged in order to carry out such a program. The combination of a high duty-factor 22 GeV JLab electron beam and the capability to measure exclusive electroproduction events at high luminosities with a large-acceptance detector would make JLab the ultimate QCD-facility at the luminosity frontier. It would be unique in possessing the capacity to explore the evolution of hadron mass and structure over the full range of distances where the transition from sQCD to pQCD is expected.

Drawing a detailed map of proton structure is important because the proton is Nature's only absolutely stable bound state. However, understanding how QCD's simplicity explains the emergence of hadron mass and structure requires investment in a facility that can deliver precision data on much more than one of Nature's hadrons. An energy-upgraded JLab facility is the only envisaged facility that could enable science to produce a sufficient quantity of precise structure data on a wide range of hadrons with distinctly different quantum numbers and thereby move into a new realm of understanding. There is elegance in simplicity and beauty in diversity. If QCD possesses both, then it presents a very plausible archetype for taking science beyond the Standard Model. In that case, nuclear physics at JLab 20+ has the potential to deliver an answer that takes science far beyond its current boundaries.

**Funding:** Work supported by: U.S. Department of Energy (contract no. DE-AC05-06OR23177) (DSC, VIM), National Science Foundation (NSF grant PHY 10011349) (RWG), and National Natural Science Foundation of China (grant no. 12135007) (CDR).

**Acknowledgments:**

This contribution is based on results obtained and insights developed through collaborations with many people, to all of whom we are greatly indebted.

**Conflicts of Interest:** The authors declare no conflict of interest.

**Abbreviations**

The following abbreviations are used in this manuscript:

CM	center-of-mass
CSM	continuum Schwinger function method
DCSB	dynamical chiral symmetry breaking
<i>d.p.</i>	data point
EHM	emergence of hadron mass
EIC	Electron-Ion Collider (at Brookhaven National Laboratory)
EicC	Electron-ion collider China
HB	Higgs boson
JLab	Thomas Jefferson National Accelerator Facility (Jefferson Laboratory)
JM	JLab-Moscow State University
lQCD	lattice-regularized quantum chromodynamics
NG (mode/boson)	Nambu-Goldstone (mode/boson)
PDFs	Particle Distribution Functions
PDG	Particle Data Group (and associated publications)
pQCD	perturbative QCD
QCD	quantum chromodynamics
RMS	root mean square
RPP	Review of Particle Properties (and associated publications)
sQCD	strong QCD
SM	Standard Model of particle physics

**References**

1. Brodsky, S.J.; et al. Strong QCD from Hadron Structure Experiments. *Int. J. Mod. Phys. E* **2020**, *29*, 2030006.
2. Binosi, D.; Mezrag, C.; Papavassiliou, J.; Roberts, C.D.; Rodriguez-Quintero, J. Process-Independent Strong Running Coupling. *Phys. Rev. D* **2017**, *96*, 054026.

3. Cui, Z.F.; Zhang, J.L.; Binosi, D.; de Soto, F.; Mezrag, C.; Papavassiliou, J.; Roberts, C.D.; Rodríguez-Quintero, J.; Segovia, J.; Zafeiropoulos, S. Effective Charge from Lattice QCD. *Chin. Phys. C* **2020**, *44*, 083102.
4. Deur, A.; Burkert, V.; Chen, J.P.; Korsch, W. Experimental Determination of the QCD Effective Charge  $\alpha_{g_1}(Q)$ . *Particles* **2022**, *5*, 171.
5. Eichmann, G.; Sanchis-Alepuz, H.; Williams, R.; Alkofer, R.; Fischer, C.S. Baryons as Relativistic Three-Quark Bound States. *Prog. Part. Nucl. Phys.* **2016**, *91*, 1.
6. Fischer, C.S. QCD at Finite Temperature and Chemical Potential from Dyson–Schwinger Equations. *Prog. Part. Nucl. Phys.* **2019**, *105*, 1.
7. Qin, S.X.; Roberts, C.D. Impressions of the Continuum Bound State Problem in QCD. *Chin. Phys. Lett.* **2020**, *37*, 121201.
8. Roberts, C.D.; Schmidt, S.M. Reflections upon the Emergence of Hadronic Mass. *Eur. Phys. J. ST* **2020**, *229*, 3319.
9. Roberts, C.D. Empirical Consequences of Emergent Mass. *Symmetry* **2020**, *12*, 1468.
10. Roberts, C.D. On Mass and Matter. *AAPPS Bulletin* **2021**, *31*, 6.
11. Roberts, C.D.; Richards, D.G.; Horn, T.; Chang, L. Insights into the Emergence of Mass from Studies of Pion and Kaon Structure. *Prog. Part. Nucl. Phys.* **2021**, *120*, 103883.
12. Binosi, D. Emergent Hadron Mass in Strong Dynamics. *Few Body Syst.* **2022**, *63*, 42.
13. Papavassiliou, J. Emergence of Mass in the Gauge Sector of QCD. *Chin. Phys. C* **2022**, *46*, 112001.
14. Ding, M.; Roberts, C.D.; Schmidt, S.M. Emergence of Hadron Mass and Structure – arXiv:2211.07763 [hep-ph]. *Particles* **2022**, *5*, in press.
15. Ferreira, M.N.; Papavassiliou, J. Gauge Sector Dynamics in QCD – arXiv:2301.02314 [hep-ph] **2023**.
16. Blum, T.; et al. Domain Wall QCD with Physical Quark Masses. *Phys. Rev. D* **2016**, *93*, 074505.
17. Boyle, P.A.; et al. Low Energy Constants of SU(2) Partially Quenched Chiral Perturbation Theory from  $N_f=2+1$  Domain Wall QCD. *Phys. Rev. D* **2016**, *93*, 054502.
18. Boyle, P.A.; Del Debbio, L.; Jüttner, A.; Khamseh, A.; Sanfilippo, F.; Tsang, J.T. The Decay Constants  $f_D$  and  $f_{D_s}$  in the Continuum Limit of  $N_f = 2 + 1$  Domain Wall Lattice QCD. *JHEP* **2017**, *12*, 008.
19. Gao, F.; Qin, S.X.; Roberts, C.D.; Rodríguez-Quintero, J. Locating the Gribov Horizon. *Phys. Rev. D* **2018**, *97*, 034010.
20. Oliveira, O.; Silva, P.J.; Skullerud, J.L.; Sternbeck, A. Quark Propagator with Two Flavors of O(a)-Improved Wilson Fermions. *Phys. Rev. D* **2019**, *99*, 094506.
21. Boucaud, P.; De Soto, F.; Raya, K.; Rodríguez-Quintero, J.; Zafeiropoulos, S. Discretization Effects on Renormalized Gauge-Field Green’s Functions, Scale Setting, and the Gluon Mass. *Phys. Rev. D* **2018**, *98*, 114515.
22. Zafeiropoulos, S.; Boucaud, P.; De Soto, F.; Rodríguez-Quintero, J.; Segovia, J. Strong Running Coupling from the Gauge Sector of Domain Wall Lattice QCD with Physical Quark Masses. *Phys. Rev. Lett.* **2019**, *122*, 162002.
23. Aguilar, A.C.; De Soto, F.; Ferreira, M.N.; Papavassiliou, J.; Rodríguez-Quintero, J. Infrared Facets of the Three-Gluon Vertex. *Phys. Lett. B* **2021**, *818*, 136352.
24. Aguilar, A.C.; Ambrósio, C.O.; De Soto, F.; Ferreira, M.N.; Oliveira, B.M.; Papavassiliou, J.; Rodríguez-Quintero, J. Ghost Dynamics in the Soft Gluon Limit. *Phys. Rev. D* **2021**, *104*, 054028.
25. Pinto-Gómez, F.; De Soto, F.; Ferreira, M.N.; Papavassiliou, J.; Rodríguez-Quintero, J. Lattice Three-Gluon Vertex in Extended Kinematics: Planar Degeneracy – arXiv:2208.01020 [hep-ph] **2022**.
26. Aznauryan, I.G.; et al. Studies of Nucleon Resonance Structure in Exclusive Meson Electroproduction. *Int. J. Mod. Phys. E* **2013**, *22*, 1330015.
27. Horn, T.; Roberts, C.D. The Pion: an Enigma within the Standard Model. *J. Phys. G* **2016**, *43*, 073001.
28. Burkert, V.D.; Roberts, C.D. Colloquium: Roper Resonance: Toward a Solution to the Fifty-Year Puzzle. *Rev. Mod. Phys.* **2019**, *91*, 011003.
29. Burkert, V.D. Nucleon Resonances and Transition Form Factors **2022**. [arXiv:hep-ph/2212.08980].
30. Beričič, J.; et al. New Insight in the  $Q^2$ -Dependence of Proton Generalized Polarizabilities. *Phys. Rev. Lett.* **2019**, *123*, 192302.
31. Blomberg, A.; et al. Virtual Compton Scattering Measurements in the Nucleon Resonance Region. *Eur. Phys. J. A* **2019**, *55*, 182.
32. Mihovilović, M.; et al. First Measurement of Proton’s Charge Form Factor at Very Low  $Q^2$  with Initial State Radiation. *Phys. Lett. B* **2017**, *771*, 194.
33. Frišič, I.; et al. Measurement of the  $p(e, e'\pi^+)n$  Reaction Close to Threshold and at Low  $Q^2$ . *Phys. Lett. B* **2017**, *766*, 301.
34. Bernauer, J.C.; et al. Electric and Magnetic Form Factors of the Proton. *Phys. Rev. C* **2014**, *90*, 015206.
35. Sparveris, N.; et al. Measurements of the  $\gamma^*p \rightarrow \Delta$  Reaction at Low  $Q^2$ . *Eur. Phys. J. A* **2013**, *49*, 136.
36. Bevan, A.J.; et al. The Physics of the B Factories. *Eur. Phys. J. C* **2014**, *74*, 3026.
37. Altmannshofer, W.; et al. The Belle II Physics Book. *PTEP* **2019**, *2019*, 123C01. [Erratum: PTEP 2020, 029201 (2020)].
38. Burkert, V.D. Jefferson Lab at 12 GeV: The Science Program. *Ann. Rev. Nucl. Part. Sci.* **2018**, *68*, 405.
39. Barabanov, M.Y.; et al. Diquark Correlations in Hadron Physics: Origin, Impact and Evidence. *Prog. Part. Nucl. Phys.* **2021**, *116*, 103835.
40. Accardi, A.; et al. An Experimental Program with High Duty-Cycle Polarized and Unpolarized Positron Beams at Jefferson Lab. *Eur. Phys. J. A* **2021**, *57*, 261.
41. Aguilar, A.C.; et al. Pion and Kaon Structure at the Electron-Ion Collider. *Eur. Phys. J. A* **2019**, *55*, 190.

42. Abdul Khalek, R.; et al. Science Requirements and Detector Concepts for the Electron-Ion Collider: EIC Yellow Report. *Nucl. Phys. A* **2022**, *1026*, 122447.
43. Arrington, J.; et al. Revealing the Structure of Light Pseudoscalar Mesons at the Electron-Ion Collider. *J. Phys. G* **2021**, *48*, 075106.
44. Chen, X.; Guo, F.K.; Roberts, C.D.; Wang, R. Selected Science Opportunities for the EIC. *Few Body Syst.* **2020**, *61*, 43.
45. Anderle, D.P.; et al. Electron-Ion Collider in China. *Front. Phys. (Beijing)* **2021**, *16*, 64701.
46. Quintans, C. The New AMBER Experiment at the CERN SPS. *Few Body Syst.* **2022**, *63*, 72.
47. Mokeev, V.I.; Carman, D.S. Photo- and Electrocouplings of Nucleon Resonances. *Few Body Syst.* **2022**, *63*, 59.
48. Carman, D.S.; Joo, K.; Mokeev, V.I. Strong QCD Insights from Excited Nucleon Structure Studies with CLAS and CLAS12. *Few Body Syst.* **2020**, *61*, 29.
49. Aznauryan, I.; Burkert, V. Electroexcitation of Nucleon Resonances. *Prog. Part. Nucl. Phys.* **2012**, *67*, 1.
50. Villano, A.N.; et al. Neutral Pion Electroproduction in the Resonance Region at High  $Q^2$ . *Phys. Rev. D* **2009**, *80*, 035203.
51. Dalton, M.M.; et al. Electroproduction of  $\eta$  Mesons in the  $S_{11}(1535)$  Resonance Region at High Momentum Transfer. *Phys. Rev. C* **2009**, *80*, 015205.
52. Anikin, I.V.; Braun, V.M.; Offen, N. Electroproduction of the  $N^*(1535)$  Nucleon Resonance in QCD. *Phys. Rev. D* **2015**, *92*, 014018.
53. Giannini, M.M.; Santopinto, E. The Hypercentral Constituent Quark Model and its Application to Baryon Properties. *Chin. J. Phys.* **2015**, *53*, 020301.
54. Braun, V.M. Hadron Wave Functions from Lattice QCD. *Few Body Syst.* **2016**, *57*, 1019.
55. Aznauryan, I.G.; Burkert, V.D. Electroexcitation of Nucleon Resonances in a Light-Front Relativistic Quark Model. *Few Body Syst.* **2018**, *59*, 98.
56. Qin, S.X.; Roberts, C.D.; Schmidt, S.M. Poincaré-Covariant Analysis of Heavy-Quark Baryons. *Phys. Rev. D* **2018**, *97*, 114017.
57. Ramalho, G. Quark Model Calculations of Transition Form Factors at High Photon Virtualities. *EPJ Web Conf.* **2020**, *241*, 02007.
58. Lyubovitskij, V.E.; Schmidt, I. Nucleon Resonances with Higher Spins in Soft-Wall AdS/QCD. *Phys. Rev. D* **2020**, *102*, 094008.
59. Raya, K.; Gutiérrez-Guerrero, L.X.; Bashir, A.; Chang, L.; Cui, Z.F.; Lu, Y.; Roberts, C.D.; Segovia, J. Dynamical Diquarks in the  $\gamma^{(*)} p \rightarrow N(1535)\frac{1}{2}^-$  Transition. *Eur. Phys. J. A* **2021**, *57*, 266.
60. Liu, L.; Chen, C.; Roberts, C.D. Wave Functions of  $(I, J^P) = (\frac{1}{2}, \frac{3}{2}^{\mp})$  Baryons – arXiv:2208.12353 [hep-ph] **2022**.
61. Liu, L.; Chen, C.; Lu, Y.; Roberts, C.D.; Segovia, J. Composition of Low-Lying  $J = 3/2^{\pm}$   $\Delta$ -Baryons. *Phys. Rev. D* **2022**, *105*, 114047.
62. Blin, A.N.H.; Melnitchouk, W.; Mokeev, V.I.; Burkert, V.D.; Chesnokov, V.V.; Pilloni, A.; Szczepaniak, A.P. Resonant Contributions to Inclusive Nucleon Structure Functions from Exclusive Meson Electroproduction data. *Phys. Rev. C* **2021**, *104*, 025201.
63. Hiller Blin, A.N.; et al. Nucleon Resonance Contributions to Unpolarised Inclusive Electron Scattering. *Phys. Rev. C* **2019**, *100*, 035201.
64. Klimenko, V.; et al. Inclusive Electron Scattering in the Resonance Region from a Hydrogen Target with CLAS12 (in progress) **2023**.
65. Wilson, D.J.; Cloet, I.C.; Chang, L.; Roberts, C.D. Nucleon and Roper Electromagnetic Elastic and Transition Form Factors. *Phys. Rev. C* **2012**, *85*, 025205.
66. Segovia, J.; Chen, C.; Cloet, I.C.; Roberts, C.D.; Schmidt, S.M.; Wan, S.L. Elastic and Transition Form Factors of the  $\Delta(1232)$ . *Few Body Syst.* **2014**, *55*, 1.
67. Mokeev, V.I.; et al. New Results from the Studies of the  $N(1440)1/2^+$ ,  $N(1520)3/2^-$ , and  $\Delta(1620)1/2^-$  Resonances in Exclusive  $ep \rightarrow e'p'\pi^+\pi^-$  Electroproduction with the CLAS Detector. *Phys. Rev. C* **2016**, *93*, 025206.
68. Segovia, J.; Cloet, I.C.; Roberts, C.D.; Schmidt, S.M. Nucleon and  $\Delta$  Elastic and Transition Form Factors. *Few Body Syst.* **2014**, *55*, 1185.
69. Segovia, J.; El-Bennich, B.; Rojas, E.; Cloet, I.C.; Roberts, C.D.; Xu, S.S.; Zong, H.S. Completing the Picture of the Roper Resonance. *Phys. Rev. Lett.* **2015**, *115*, 171801.
70. Segovia, J.; Roberts, C.D. Dissecting Nucleon Transition Electromagnetic Form Factors. *Phys. Rev. C* **2016**, *94*, 042201(R).
71. Chen, C.; Lu, Y.; Binosi, D.; Roberts, C.D.; Rodríguez-Quintero, J.; Segovia, J. Nucleon-to-Roper Electromagnetic Transition Form Factors at Large  $Q^2$ . *Phys. Rev. D* **2019**, *99*, 034013.
72. Burkert, V.D.; Mokeev, V.I.; Ishkhanov, B.S. The Nucleon Resonance Structure from the  $\pi^+\pi^-p$  Electroproduction Reaction off Protons. *Moscow Univ. Phys. Bull.* **2019**, *74*, 243. [Vestn. Mosk. Univ. Ser. III Fiz. Astron. **74** (2019) pp. 28-38].
73. Roberts, C.D. Resonance Electroproduction and the Origin of Mass. *EPJ Web Conf.* **2020**, *241*, 02008.
74. Lu, Y.; Chen, C.; Cui, Z.F.; Roberts, C.D.; Schmidt, S.M.; Segovia, J.; Zong, H.S. Transition Form Factors:  $\gamma^* + p \rightarrow \Delta(1232)$ ,  $\Delta(1600)$ . *Phys. Rev. D* **2019**, *100*, 034001.
75. Mokeev, V.I. Two Pion Photo- and Electroproduction with CLAS. *EPJ Web Conf.* **2020**, *241*, 03003.
76. Workman, R.L.; et al. Review of Particle Physics. *PTEP* **2022**, *2022*, 083C01.
77. Binosi, D.; Chang, L.; Papavassiliou, J.; Qin, S.X.; Roberts, C.D. Natural Constraints on the Gluon-Quark Vertex. *Phys. Rev. D* **2017**, *95*, 031501(R).
78. Chang, L.; Cloet, I.C.; Roberts, C.D.; Schmidt, S.M.; Tandy, P.C. Pion electromagnetic form factor at spacelike momenta. *Phys. Rev. Lett.* **2013**, *111*, 141802.
79. Cui, Z.F.; Chen, C.; Binosi, D.; de Soto, F.; Roberts, C.D.; Rodríguez-Quintero, J.; Schmidt, S.M.; Segovia, J. Nucleon Elastic Form Factors at Accessible Large Spacelike Momenta. *Phys. Rev. D* **2020**, *102*, 014043.

80. Ripani, M.; et al. A Phenomenological Description of  $\pi^- \Delta^{++}$  Photoproduction and Electroproduction in Nucleon Resonance Region. *Nucl. Phys. A* **2000**, *672*, 220.
81. Burkert, V.D.; et al. Isobar Channels in the Production of  $\pi^+ \pi^-$  Pairs on a Proton by Virtual Photons. *Phys. Atom. Nucl.* **2007**, *70*, 427.
82. Mokeev, V.I.; Burkert, V.D.; Lee, T.S.H.; Elouadrhiri, L.; Fedotov, G.V.; Ishkhanov, B.S. Model Analysis of the  $p\pi^+ \pi^-$  Electroproduction Reaction on the Proton. *Phys. Rev. C* **2009**, *80*, 045212.
83. Mokeev, V.I.; et al. Experimental Study of the  $P_{11}(1440)$  and  $D_{13}(1520)$  Resonances from CLAS Data on  $ep \rightarrow e' \pi^+ \pi^- p'$ . *Phys. Rev. C* **2012**, *86*, 035203.
84. Roberts, C.D.; Williams, A.G. Dyson-Schwinger Equations and their Application to Hadronic Physics. *Prog. Part. Nucl. Phys.* **1994**, *33*, 477.
85. Cornwall, J.M. Dynamical Mass Generation in Continuum QCD. *Phys. Rev. D* **1982**, *26*, 1453.
86. Schwinger, J.S. Gauge Invariance and Mass. *Phys. Rev.* **1962**, *125*, 397.
87. Schwinger, J.S. Gauge Invariance and Mass. 2. *Phys. Rev.* **1962**, *128*, 2425.
88. Aguilar, A.C.; Binosi, D.; Papavassiliou, J. Gluon and Ghost Propagators in the Landau Gauge: Deriving Lattice Results from Schwinger-Dyson Equations. *Phys. Rev. D* **2008**, *78*, 025010.
89. Boucaud, P.; Leroy, J.P.; Le-Yaouanc, A.; Micheli, J.; Pene, O.; Rodríguez-Quintero, J. The Infrared Behaviour of the Pure Yang-Mills Green Functions. *Few Body Syst.* **2012**, *53*, 387.
90. Aguilar, A.C.; Binosi, D.; Papavassiliou, J. The Gluon Mass Generation Mechanism: A Concise Primer. *Front. Phys. China* **2016**, *11*, 111203.
91. Aguilar, A.C.; Ferreira, M.N.; Papavassiliou, J. Exploring Smoking-Gun Signals of the Schwinger Mechanism in QCD. *Phys. Rev. D* **2022**, *105*, 014030.
92. Aguilar, A.C.; De Soto, F.; Ferreira, M.N.; Papavassiliou, J.; Pinto-Gómez, F.; Roberts, C.D.; Rodríguez-Quintero, J. Schwinger Mechanism for Gluons from Lattice QCD **2022**. [[arXiv:hep-ph/2211.12594](https://arxiv.org/abs/2211.12594)].
93. Grunberg, G. Renormalization Scheme Independent QCD and QED: The Method of Effective Charges. *Phys. Rev. D* **1984**, *29*, 2315.
94. Grunberg, G. On Some Ambiguities in the Method of Effective Charges. *Phys. Rev. D* **1989**, *40*, 680.
95. Bjorken, J.D. Applications of the Chiral  $U(6) \times (6)$  Algebra of Current Densities. *Phys. Rev.* **1966**, *148*, 1467.
96. Bjorken, J.D. Inelastic Scattering of Polarized Leptons from Polarized Nucleons. *Phys. Rev. D* **1970**, *1*, 1376.
97. Gell-Mann, M. A Schematic Model of Baryons and Mesons. *Phys. Lett.* **1964**, *8*, 214.
98. Eichmann, G.; Ramalho, G. Nucleon Resonances in Compton Scattering. *Phys. Rev. D* **2018**, *98*, 093007.
99. Ding, M.; Raya, K.; Binosi, D.; Chang, L.; Roberts, C.D.; Schmidt, S.M. Symmetry, Symmetry Breaking, and Pion Parton Distributions. *Phys. Rev. D* **2020**, *101*, 054014.
100. Chen, C.; Roberts, C.D. Nucleon Axial Form Factor at Large Momentum Transfers. *Eur. Phys. J. A* **2022**, *58*, 206.
101. Maris, P.; Roberts, C.D.; Tandy, P.C. Pion Mass and Decay Constant. *Phys. Lett. B* **1998**, *420*, 267.
102. Maris, P.; Roberts, C.D. Pi- and K Meson Bethe-Salpeter Amplitudes. *Phys. Rev. C* **1997**, *56*, 3369.
103. Höll, A.; Krassnigg, A.; Roberts, C.D. Pseudoscalar Meson Radial Excitations. *Phys. Rev. C* **2004**, *70*, 042203(R).
104. Brodsky, S.J.; Roberts, C.D.; Shrock, R.; Tandy, P.C. Confinement Contains Condensates. *Phys. Rev. C* **2012**, *85*, 065202.
105. Qin, S.X.; Roberts, C.D.; Schmidt, S.M. Ward-Green-Takahashi Identities and the Axial-Vector Vertex. *Phys. Lett. B* **2014**, *733*, 202.
106. Nambu, Y. Quasiparticles and Gauge Invariance in the Theory of Superconductivity. *Phys. Rev.* **1960**, *117*, 648.
107. Goldstone, J. Field Theories with Superconductor Solutions. *Nuovo Cim.* **1961**, *19*, 154.
108. Roberts, C.D. Perspective on the Origin of Hadron Masses. *Few Body Syst.* **2017**, *58*, 5.
109. Flambaum, V.V.; Holl, A.; Jaikumar, P.; Roberts, C.D.; Wright, S.V. Sigma Terms of Light-Quark Hadrons. *Few Body Syst.* **2006**, *38*, 31.
110. Ruiz de Elvira, J.; Hoferichter, M.; Kubis, B.; Meißner, U.G. Extracting the  $\sigma$ -Term from Low-Energy Pion-Nucleon Scattering. *J. Phys. G* **2018**, *45*, 024001.
111. Aoki, S.; et al. FLAG Review 2019. *Eur. Phys. J. C* **2020**, *80*, 113.
112. Workman, R.L.; et al. Review of Particle Physics. *PTEP* **2022**, *2022*, 083C01.
113. Obukhovskiy, I.T.; Faessler, A.; Fedorov, D.K.; Gutsche, T.; Lyubovitskij, V.E. Transition Form Factors and Helicity Amplitudes for Electroexcitation of Negative- and Positive Parity Nucleon Resonances in a Light-Front Quark Model. *Phys. Rev. D* **2019**, *100*, 094013.
114. Carman, D.S. Nucleon Resonance Structure Studies Via Exclusive KY Electroproduction. *Few Body Syst.* **2016**, *57*, 941.
115. Carman, D.S. CLAS  $N^*$  Excitation Results from Pion and Kaon Electroproduction. *Few Body Syst.* **2018**, *59*, 82.
116. CLAS Physics Database. <https://clasweb.jlab.org/physicsdb/>.
117. Chesnokov, V.V.; Golubenko, A.A.; Ishkhanov, B.S.; Mokeev, V.I. CLAS Database for Studies of the Structure of Hadrons in Electromagnetic Processes. *Phys. Part. Nucl.* **2022**, *53*, 184.
118. Aznauryan, I.G. Multipole Amplitudes of Pion Photoproduction on Nucleons up to 2-GeV Within Dispersion Relations and Unitary Isobar Model. *Phys. Rev. C* **2003**, *67*, 015209.

119. Aznauryan, I.G.; Burkert, V.D.; Fedotov, G.V.; Ishkhanov, B.S.; Mokeev, V.I. Electroexcitation of Nucleon Resonances at  $Q^2 = 0.65$  (GeV/c)<sup>2</sup> from a Combined Analysis of Single- and Double-Pion Electroproduction Data. *Phys. Rev. C* **2005**, *72*, 045201.
120. Arndt, R.; Briscoe, W.; Strakovsky, I.; Workman, R. Partial-Wave Analysis And Spectroscopy: From  $\pi N$  Scattering To Pion-Electroproduction. *eConf* **2007**, *C070910*, 166.
121. Drechsel, D.; Kamalov, S.S.; Tiator, L. Unitary Isobar Model - MAID2007. *Eur. Phys. J. A* **2007**, *34*, 69.
122. Aznauryan, I.G.; et al. Electroexcitation of Nucleon Resonances from CLAS Data on Single Pion Electroproduction. *Phys. Rev. C* **2009**, *80*, 055203.
123. Tiator, L.; Drechsel, D.; Kamalov, S.S.; Vanderhaeghen, M. Electromagnetic Excitation of Nucleon Resonances. *Eur. Phys. J. ST* **2011**, *198*, 141.
124. Park, K.; et al. Measurements of  $ep \rightarrow e' \pi^+ n$  at  $W = 1.6 - 2.0$  GeV and Extraction of Nucleon Resonance Electrocouplings at CLAS. *Phys. Rev. C* **2015**, *91*, 045203.
125. Tiator, L.; Döring, M.; Workman, R.L.; Hadžimehmedović, M.; Osmanović, H.; Omerović, R.; Stahov, J.; Švarc, A. Baryon Transition Form Factors at the Pole. *Phys. Rev. C* **2016**, *94*, 065204.
126. Tiator, L.; Workman, R.L.; Wunderlich, Y.; Habertzettl, H. Amplitude Reconstruction from Complete Electroproduction Experiments and Truncated Partial-Wave Expansions. *Phys. Rev. C* **2017**, *96*, 025210.
127. Tiator, L. The MAID Legacy and Future. *Few Body Syst.* **2018**, *59*, 21.
128. Knochlein, G.; Drechsel, D.; Tiator, L. Photoproduction and Electroproduction of  $\eta$  Mesons. *Z. Phys. A* **1995**, *352*, 327.
129. Chiang, W.T.; Yang, S.N.; Tiator, L.; Drechsel, D. An Isobar Model for  $\eta$  Photoproduction and Electroproduction on the Nucleon. *Nucl. Phys. A* **2002**, *700*, 429.
130. Chiang, W.T.; Yang, S.N.; Drechsel, D.; Tiator, L. An Isobar Model Study of  $\eta$  Photoproduction and Electroproduction. *PiN Newslett.* **2002**, *16*, 299.
131. Aznauryan, I. Resonance Contributions to  $\eta$  Photoproduction on Protons Found Using Dispersion Relations and an Isobar Model. *Phys. Rev. C* **2003**, *68*, 065204.
132. Kamano, H. Electromagnetic  $N^*$  Transition Form Factors in the ANL-Osaka Dynamical Coupled-Channels Approach. *Few Body Syst.* **2018**, *59*, 24.
133. Mai, M.; Döring, M.; Granados, C.; Habertzettl, H.; Hergenrath, J.; Meißner, U.G.; Rönchen, D.; Strakovsky, I.; Workman, R. Coupled-Channels Analysis of Pion and  $\eta$  Electroproduction within the Jülich-Bonn-Washington Model. *Phys. Rev. C* **2022**, *106*, 015201.
134. Mai, M.; Döring, M.; Granados, C.; Habertzettl, H.; Meißner, U.G.; Rönchen, D.; Strakovsky, I.; Workman, R. Jülich-Bonn-Washington Model for Pion Electroproduction Multipoles. *Phys. Rev. C* **2021**, *103*, 065204.
135. Hwang, S.; et al. Measurement of 3-Body Hadronic Reactions with HypTPC at J-PARC. *JPS Conf. Proc.* **2015**, *8*, 022008.
136. Hicks, K.H.; Sako, H.; et al. 3-Body Hadronic Reactions for New Aspects of Baryon Spectroscopy, 2012.
137. Aznauryan, I.; et al. Electroexcitation of Nucleon Resonances from CLAS Data on Single Pion Electroproduction. *Phys. Rev. C* **2009**, *80*, 055203.
138. Mokeev, V.I. New Opportunities for Insight into the Emergence of Hadron Mass from Studies of Nucleon Resonance Electroexcitation. In Proceedings of the Fall 2022 Meeting of the APS Division of Nuclear Physics, 2022.
139. Mokeev, V.I. Nucleon Resonance Electrocouplings and the Emergence of Hadron Mass. In Proceedings of the Baryons 2022 - International Conference on the Structure of Baryons, 2022.
140. Dugger, M.; et al.  $\pi^+$  Photoproduction on the Proton for Photon Energies from 0.725 to 2.875 GeV. *Phys. Rev. C* **2009**, *79*, 065206.
141. Aznauryan, I.G.; Burkert, V.D. Extracting Meson-Baryon Contributions to the Electroexcitation of the  $N(1675)_{\frac{5}{2}^-}$  Nucleon Resonance. *Phys. Rev. C* **2015**, *92*, 015203.
142. Chen, C.; Fischer, C.S.; Roberts, C.D.; Segovia, J. Nucleon Axial-Vector and Pseudoscalar Form Factors and PCAC Relations. *Phys. Rev. D* **2022**, *105*, 094022.
143. Chang, L.; Cloet, I.C.; Cobos-Martinez, J.J.; Roberts, C.D.; Schmidt, S.M.; Tandy, P.C. Imaging Dynamical Chiral Symmetry Breaking: Pion Wave Function on the Light Front. *Phys. Rev. Lett.* **2013**, *110*, 132001.
144. Raya, K.; Chang, L.; Bashir, A.; Cobos-Martinez, J.J.; Gutiérrez-Guerrero, L.X.; Roberts, C.D.; Tandy, P.C. Structure of the neutral pion and its electromagnetic transition form factor. *Phys. Rev. D* **2016**, *93*, 074017.
145. Mokeev, V.I. Insight into EHM from Results on Electroexcitation of  $\Delta(1600)_{3/2^+}$  Resonance. In Proceedings of the Workshop on perceiving the Emergence of Hadron Mass through AMBER @ CERN - VII, 2022.
146. Isupov, E.L.; et al. Measurements of  $ep \rightarrow e' \pi^+ \pi^- p'$  Cross Sections with CLAS at  $1.40 \text{ GeV} < W < 2.0 \text{ GeV}$  and  $2.0 \text{ GeV}^2 < Q^2 < 5.0 \text{ GeV}^2$ . *Phys. Rev. C* **2017**, *96*, 025209.
147. Trivedi, A. Measurement of New Observables from the  $\pi^+ \pi^- p$  Electroproduction Off the Proton. *Few Body Syst.* **2019**, *60*, 5.
148. Mokeev, V.I.; et al. Evidence for the  $N'(1720)_{3/2^+}$  Nucleon Resonance from Combined Studies of CLAS  $\pi^+ \pi^- p$  Photo- and Electroproduction Data. *Phys. Lett. B* **2020**, *805*, 135457.
149. Mokeev, V.I.; Carman, D.S. New Baryon States in Exclusive Meson Photo-/Electroproduction with CLAS. *Rev. Mex. Fis. Suppl.* **2022**, *3*, 0308024.
150. Burkert, V.D.; et al. The CLAS12 Spectrometer at Jefferson Laboratory. *Nucl. Instrum. Meth. A* **2020**, *959*, 163419.
151. Gothe, R.W.; et al. Nucleon Resonance Studies with CLAS12. JLab Experiment E12-09-003.
152. Carman, D.S.; et al. Exclusive  $N^* \rightarrow KY$  Studies with CLAS12. JLab Experiment E12-06-108A.

- 
153. D'Angelo, A.; et al. A Search for Hybrid Baryons in Hall B with CLAS12. JLab Experiment E12-16-010.
  154. Carman, D.S.; et al. Beam-Recoil Transferred Polarization in  $K^+Y$  Electroproduction in the Nucleon Resonance Region with CLAS12. *Phys. Rev. C* **2022**, *105*, 065201.
  155. Burkert, V.D.  $N^*$  Experiments and Their Impact on Strong QCD Physics. *Few Body Syst.* **2018**, *59*, 57.
  156. Aznauryan, I.; Burkert, V.; Lee, T.S.; Mokeev, V. Results from the  $N^*$  program at JLab. *J. Phys. Conf. Ser.* **2011**, *299*, 012008.